International Journal of Solids and Structures 50 (2013) 3067–3088

Contents lists available at SciVerse ScienceDirect

International Journal of Solids and Structures

journal homepage: www.elsevier.com/locate/ijsolstr

Formulation of the stress fields in power law solids ahead of three-dimensional tensile cracks

Mujing Xiang [a,b], Wanlin Guo [a,*]

[a] State Key Laboratory of Mechanics and Control of Mechanical Structures, Nanjing University of Aeronautics and Astronautics, 29 Yu-Dao Street, Nanjing 210016, China
[b] R&D Institute of Pump Division of Sany, Sany Industrial Park, Xingsha Enterprise Zone, Changsha 410100, China

ARTICLE INFO

Article history:
Received 13 April 2012
Received in revised form 6 May 2013
Available online 1 June 2013

Keywords:
Three-dimensional crack
Power law plastic and creeping solids
Out-of-plane stress constraint factor T_z
Explicit formulae
Three-parameter descriptions

ABSTRACT

To accurately predict damage behavior in engineering applications, it is important to investigate the three-dimensional (3D) stress state near a real crack border. Introducing the out-of-plane stress constraint factor T_z, Guo and his colleagues derived out the 3D asymptotic fields near the tensile crack border in power law plastic (Guo, 1993a, 1993b, 1995) and creeping solids (Xiang et al., 2011). However, these theoretical solutions are presented in curves and too complicated for application. Here we formulize the 3D theoretical solutions into a set of empirical explicit formulae in the whole range of out-of-plane stress constraint from $T_z = 0$ at plane stress state to $T_z = 0.5$ at plane strain state. At the two limits of $T_z = 0$ and 0.5, the empirical formulae degrade into the two dimensional (2D) HRR (Hutchinson, 1968; Rice and Rosengren, 1968) or RR (Riedel and Rice, 1980) solutions with high accuracy. Detailed finite element analyses are performed for cracked plates with finite thickness under power law plastic and creeping conditions to verify the formulation of the asymptotic crack border stress fields. It is shown that the in-plane stress components and stress triaxiality on the ligament ahead of the crack border can be efficiently predicted by the explicit formulae. We also investigate the dominance of the formulation of stress components in the whole forward sector to give a more convenient description for wide applications. Based on the formulation, we discuss the influence of both in-plane and out-of-plane constraints. Three-parameter descriptions, such as the J–T_z–Q^T description for plastic solids proposed by Guo (2000) and the $C(t)$–T_z–Q^* description for creeping solids proposed by Xiang et al. (2011) are evaluated based on comparison of the empirical formulae and 3D finite element results. The three-parameter descriptions are shown to be necessary and efficient under large scale yielding or extensive creeping conditions in the whole forward sector of cracked plates with finite thickness.

1. Introduction

In past decades, the development of fracture mechanics and its applications have mainly been based on the asymptotic solutions of crack-tip stress fields and related dominative parameters. For two-dimensional (2D) cracks in power law plastic solids, Hutchinson (1968), Rice and Rosengren (1968) developed the nonlinear asymptotic solution for the near-tip stresses, known as the HRR solution, and showed that the magnitude of the singular leading term in the expansion of the solution is determined by the Rice J-integral (Rice, 1968). It has been recognized that the J dominated region is very small and dependent on loading type and geometrical configurations in the plane strain state (Leevers and Radon, 1982; McMeeking, 1977). In the early 1990s, inspired by the J–A_2 solution obtained by Li and Wang (1986), two-parameter descriptions were developed for consideration of the in-plane constraint caused by in-plane geometry, size and loading configurations, such as the J–T solution (Betegon and Hancock, 1991), J–Q solution (O'Dowd and Shih, 1991, 1992), and higher order solutions up to five terms were obtained (Xia et al., 1993; Yang et al., 1993). However, practical structural components have finite thicknesses, and the materials are always in a 3D stress state near a real crack border. Therefore, it is important to study the effects of 3D constraints and stress states around the 3D crack border. By introducing an out-of-plane stress constraint factor T_z (the ratio of out-of-plane stress σ_{33} over the sum of in-plane stresses σ_{11} and σ_{22}, or $T_z = \frac{\sigma_{33}}{\sigma_{11}+\sigma_{22}}$), Guo studied the asymptotic stress and strain fields near 3D crack border systematically and obtained the J–T_z solution (Guo, 1993a, 1993b, 1995), where the subscripts 1, 2 and 3 stand for x, y and z in the Cartesian coordinate system, or r, θ and z in the polar coordinate system, respectively, with z axis along the direction tangential to the crack front line. Furthermore, J–T_z–Q^T solution was proposed by Guo (2000) to consider both the in-plane and out-of-plane constraints.

* Corresponding author. Tel./fax: +86 25 84895827.
E-mail address: wlguo@nuaa.edu.cn (W. Guo).

0020-7683/$ - see front matter © 2013 Elsevier Ltd. All rights reserved.
http://dx.doi.org/10.1016/j.ijsolstr.2013.05.011

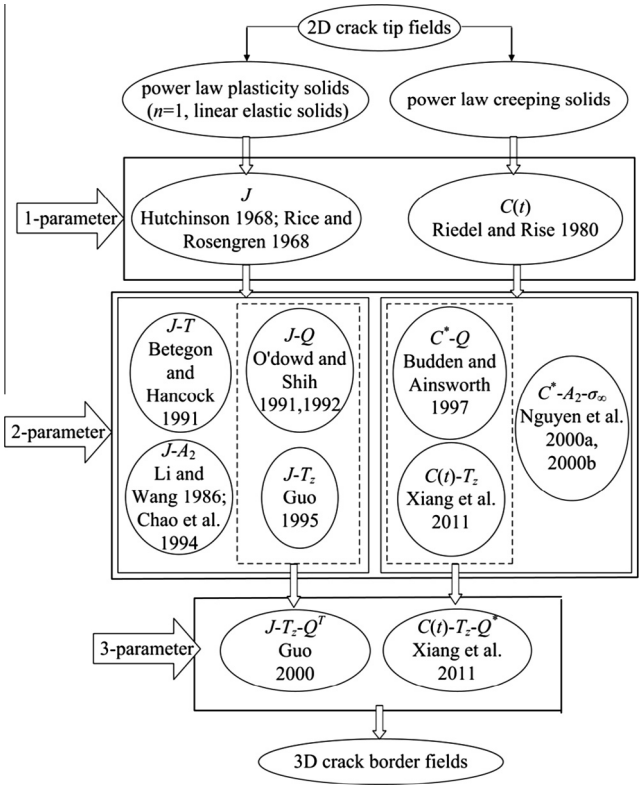

Fig. 1. Evolution in the solutions of crack-tip/border fields from 2D to 3D cracked solids.

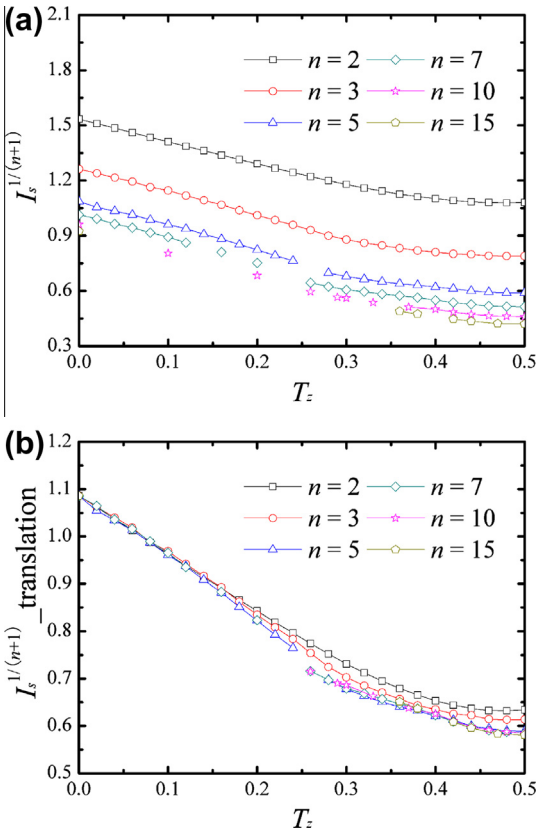

Fig. 2. Analytical results of $[I_s(T_z,n)]^{1/(n+1)}$ plotted versus T_z for different n. (a) $[I_s(T_z,n)]^{1/(n+1)}$, (b) $[I_s(T_z,n)]^{1/(n+1)}$ translated to a reference point $(0,[I_s(0,5)]^{1/(5+1)})$.

Under uniaxial tension, the elastic-power law plastic solids can be modeled by

$$\varepsilon = \frac{\sigma}{E} + \alpha\varepsilon_0\left(\frac{\sigma}{\sigma_0}\right)^{n_1}, \tag{1.1}$$

where E is Young's modulus, σ_0 is often taken to be representative of the yield strength, $\varepsilon_0 = \sigma_0/E$, n_1 and α are the plasticity exponent and coefficient in the Ramberg–Osgood constitutive relationship, respectively.

As $n_1 > 1$, the elastic strain near the crack border can be neglected because of the singularity of stresses. Then, in the vicinity of crack tip, Eq. (1.1) can be reduced to

$$\varepsilon = \alpha\varepsilon_0\left(\frac{\sigma}{\sigma_0}\right)^{n_1}. \tag{1.2}$$

Then the in-plane stress fields near the crack border in 3D power law plastic solids can be obtained as (Guo, 1995)

$$\sigma_{ij} = \sigma_0\left[\frac{J}{\alpha\varepsilon_0\sigma_0 I(T_z,n_1)r}\right]^{\frac{1}{n_1+1}}\tilde{\sigma}_{ij}(n_1,\theta,T_z), \quad (i,j=r,\theta), \tag{1.3}$$

where r and θ are polar coordinates centered at the crack border, with $\theta = 0$ corresponding to the ligament directly ahead of the crack border.

For creep fracture at high temperature, most previous works have been performed within the frame of 2D theory. At first, the crack border fields in power law creeping solids have been described by Riedel and Rice using a single parameter $C(t)$ in 2D ideal plane stress and plane strain conditions, known as the RR solution (Riedel and Rice, 1980). Then the researchers revealed that the RR solution must be also improved to consider the constraint effects caused by the 3D geometry of components and loading mode etc. Nguyen et al. (2000a, 2000b) proposed a three-term description C^*–A_2–σ_∞, in which the parameters A_2 and σ_∞ account for the constraint effect imposed by the specific geometry and loading configuration. Budden and Ainsworth (1997) introduced the Q-parameter to investigate the in-plane constraint effect in creeping solids via analogy with power law plasticity. By considering the out-of-plane stress constraint factor T_z introduced by Guo (1993a), our group derived out the 3D asymptotic fields near the tensile crack border in power law creeping solids, and proposed $C(t)$–T_z solution and $C(t)$–T_z–Q^* solution under small scale creep conditions and extensive creep conditions, respectively (Xiang et al., 2011).

Under uniaxial tension, the elastic-power law creeping solids can be modeled as

$$\dot{\varepsilon} = \frac{\dot{\sigma}}{E} + \dot{\varepsilon}_0\left(\frac{\sigma}{\sigma_0}\right)^{n_2}, \tag{1.4}$$

where E is Young's modulus, σ_0 is a reference stress, $\dot{\varepsilon}_0 = B\sigma_0^{n_2}$, n_2 and B are the creep exponent and coefficient in the Norton constitutive relationship, respectively.

In the vicinity of crack tip, Eq. (1.4) can be reduced to

$$\dot{\varepsilon} = \dot{\varepsilon}_0\left(\frac{\sigma}{\sigma_0}\right)^{n_2}. \tag{1.5}$$

Then the in-plane stress fields near the crack border in 3D creeping solids can be obtained as (Xiang et al., 2011)

$$\sigma_{ij} = \sigma_0\left[\frac{C(t)}{\dot{\varepsilon}_0\sigma_0 I(T_z,n_2)r}\right]^{\frac{1}{n_2+1}}\tilde{\sigma}_{ij}(n_2,\theta,T_z), \quad (i,j=r,\theta), \tag{1.6}$$

where r and θ are polar coordinates centered at the crack border, $\theta = 0$ corresponds to the ligament directly ahead of the crack border.

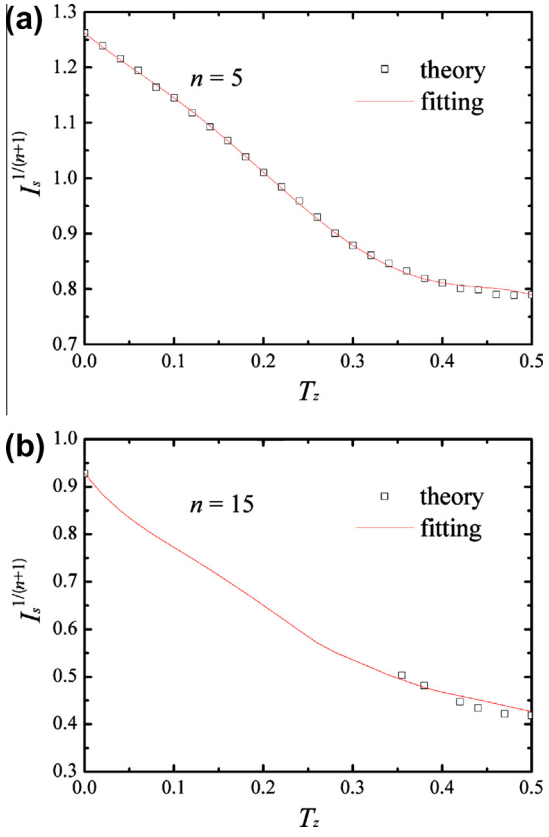

Fig. 3. Examples of $[I_s(T_z,n)]^{1/(n+1)}$ plotted versus T_z for (a) $n = 5$; (b) $n = 15$.

The diagram shown in Fig. 1 summarizes the development from 2D 1-parameter solutions to 3D 3-parameter solutions of crack border fields including both the in-plane and out-of-plane constraints in power law plastic and creeping solids. Theoretically, the solutions for crack border fields in 2D and 3D solids become relatively complete. However, they are obtained analytically with a complicated iterating process being involved and presented in curves, no explicit formulae for these solutions have been proposed yet. Furthermore, the iteration convergence in obtaining the numerical solutions is somewhat slower for low T_z and larger n when considering the out-of-plane constraint effect, thus hindering wide engineering applications of these nonlinear solutions, especially in 3D power law solids.

In this paper, we formulize the 2D and 3D solutions under power law conditions into explicit formulae by empirically fitting the corresponding theoretical solutions. As the typical value for n_1 and n_2 are between 2 and 20 for most metals, our formulation is concentrated to the range of $2 < (n_1, n_2) < 20$. Comparison with detailed 3D finite element analyses performed for single-edge cracked specimens shows that the formulation is efficient for representation of the distributions of in-plane stresses and stress triaxiality on the ligament ahead of the crack border in both of the plastic and creeping plates with finite thickness in small yielding/creeping situations. Under large yielding/creeping conditions, in-plane constraint has to be considered and the three-parameter descriptions of J–T_z–Q^T for plastic solids or $C(t)$–T_z–Q^* for creeping solids based on the formulation are necessary and efficient to predict the 3D stress fields in the whole forward sector of through-the-thickness cracks.

2. Formulation

For convenience, the angular distribution of stress $\tilde{\sigma}'_{ij}(n,\theta,T_z)$ normalized by $\tilde{\sigma}_{\theta\theta}(n,0,T_z)$ is used in the following formulation. Then Eqs. (1.3) and (1.6) can be rearranged as

$$\begin{aligned}\sigma_{ij} &= \sigma_0\left[\frac{J}{\alpha\varepsilon_0\sigma_0 I(T_z,n_1)r}\right]^{\frac{1}{n_1+1}}\tilde{\sigma}'_{ij}(n_1,\theta,T_z)\\ &= \sigma_0\left[\frac{J}{\alpha\varepsilon_0\sigma_0\frac{I(T_z,n)}{\tilde{\sigma}_{\theta\theta}(n,0,T_z)^{n_1+1}}r}\right]^{\frac{1}{n_1+1}}\frac{\tilde{\sigma}_{ij}(n_1,\theta,T_z)}{\tilde{\sigma}_{\theta\theta}(n_1,0,T_z)}\\ &= \sigma_0\left[\frac{J}{\alpha\varepsilon_0\sigma_0 I_s(T_z,n_1)r}\right]^{\frac{1}{n_1+1}}\tilde{\sigma}'_{ij}(n_1,\theta,T_z),\quad \text{(plastic solids)},\end{aligned}\tag{2.1}$$

$$\begin{aligned}\sigma_{ij} &= \sigma_0\left[\frac{C(t)}{\dot{\varepsilon}_0\sigma_0 I(T_z,n_2)r}\right]^{\frac{1}{n_2+1}}\tilde{\sigma}_{ij}(n_2,\theta,T_z)\\ &= \sigma_0\left[\frac{C(t)}{\dot{\varepsilon}_0\sigma_0\frac{I(T_z,n)}{\tilde{\sigma}_{\theta\theta}(n,0,T_z)^{n_2+1}}r}\right]^{\frac{1}{n_2+1}}\frac{\tilde{\sigma}_{ij}(n_2,\theta,T_z)}{\tilde{\sigma}_{\theta\theta}(n_2,0,T_z)}\\ &= \sigma_0\left[\frac{C(t)}{\dot{\varepsilon}_0\sigma_0 I_s(T_z,n_2)r}\right]^{\frac{1}{n_2+1}}\tilde{\sigma}'_{ij}(n_2,\theta,T_z),\quad \text{(creeping solids)},\end{aligned}\tag{2.2}$$

where $I_s(T_z,n)=\frac{I(T_z,n)}{\tilde{\sigma}_{\theta\theta}(n,0,T_z)^{n+1}}$, $\tilde{\sigma}'_{ij}(n,\theta,T_z)=\frac{\tilde{\sigma}_{ij}(n,\theta,T_z)}{\tilde{\sigma}_{\theta\theta}(n,0,T_z)}$.

For mode I crack problems, it is important to investigate the stress states in the forward sector of the crack border, and Eqs. (2.1) and (2.2) indicate that the singular term of in-plane stress components is not only dominated by the J integral or $C(t)$, but also affected by the out-of-plane stress constraint factor T_z through both the amplitude factor $I_s(T_z,n)$ and angular distribution of stress $\tilde{\sigma}'_{ij}(n,\theta,T_z)$ for given materials and loads. Obviously, $\sigma_{\theta\theta}$ on the ligament directly ahead of the crack border ($\theta = 0$) can be reduced to

$$\sigma_{\theta\theta} = \sigma_0\left[\frac{J}{\alpha\varepsilon_0\sigma_0 I_s(T_z,n_1)r}\right]^{\frac{1}{n_1+1}},\quad \text{(plastic solids)},\tag{2.3}$$

$$\sigma_{\theta\theta} = \sigma_0\left[\frac{C(t)}{\dot{\varepsilon}_0\sigma_0 I_s(T_z,n_2)r}\right]^{\frac{1}{n_2+1}},\quad \text{(creeping solids)}.\tag{2.4}$$

2.1. Solution of $I_s(T_z,n)$

As the stress-state-related parameters $I(T_z,n)$ and $\tilde{\sigma}_{\theta\theta}(n,0,T_z)$ can be solved analytically in a combination of the fourth order Runge–Kutta method and a shooting procedure (Guo, 1993b; Xiang et al., 2011), we can obtain the theoretical results of $[I_s(T_z,n)]^{1/(n+1)}$ plotted versus T_z for different n, as shown in Fig. 2(a).

For larger n (>10), it is hard to converge the iteration process in the theoretical solutions in some ranges of T_z. However, Fig. 2(a) presents that there is a simple relation between $[I_s(T_z,n)]^{1/(n+1)}$ and T_z for us to make use of to predict the divergent ranges for larger n. It is interesting to find that with a translation of the $[I_s(T_z,n)]^{1/(n+1)}$–T_z curves to a reference point, $(0,[I_s(0,5)]^{1/(5+1)})$, the curves for $n > 10$ almost collapse into a single curve, as shown in Fig. 2(b). This means that the relation between $[I_s(T_z,n)]^{1/(n+1)}$ and T_z for larger n can be approximated by translating the curve for $n = 10$ from $(0,[I_s(0,10)]^{1/(10+1)})$ to $(0,[I_s(0,n_{\text{larger}})]^{1/(n\text{larger}+1)})$, while $[I_s(0,n_{\text{larger}})]^{1/(n\text{larger}+1)}$ can be solved out analytically up to $n = 20$ following the procedure used by Guo (1993b) and Xiang et al. (2011).

For $n \leqslant 10$, we adopt quintic curves to fit $[I_s(T_z,n)]^{1/(n+1)}$ in all the range of $0 \leqslant T_z \leqslant 0.5$), and it is necessary and sufficient to select six points, namely $T_z = 0$, 0.1, 0.2, 0.3, 0.4 and 0.5, to determine the quintic curves as

$$[I_s(T_z,n)]^{1/(n+1)} = aT_z^5 + bT_z^4 + cT_z^3 + dT_z^2 + eT_z + f,\quad (n \leqslant 10),\tag{2.5}$$

where (let I_{Tz} represents $[I_s(T_z,n)]^{1/(n+1)}$),

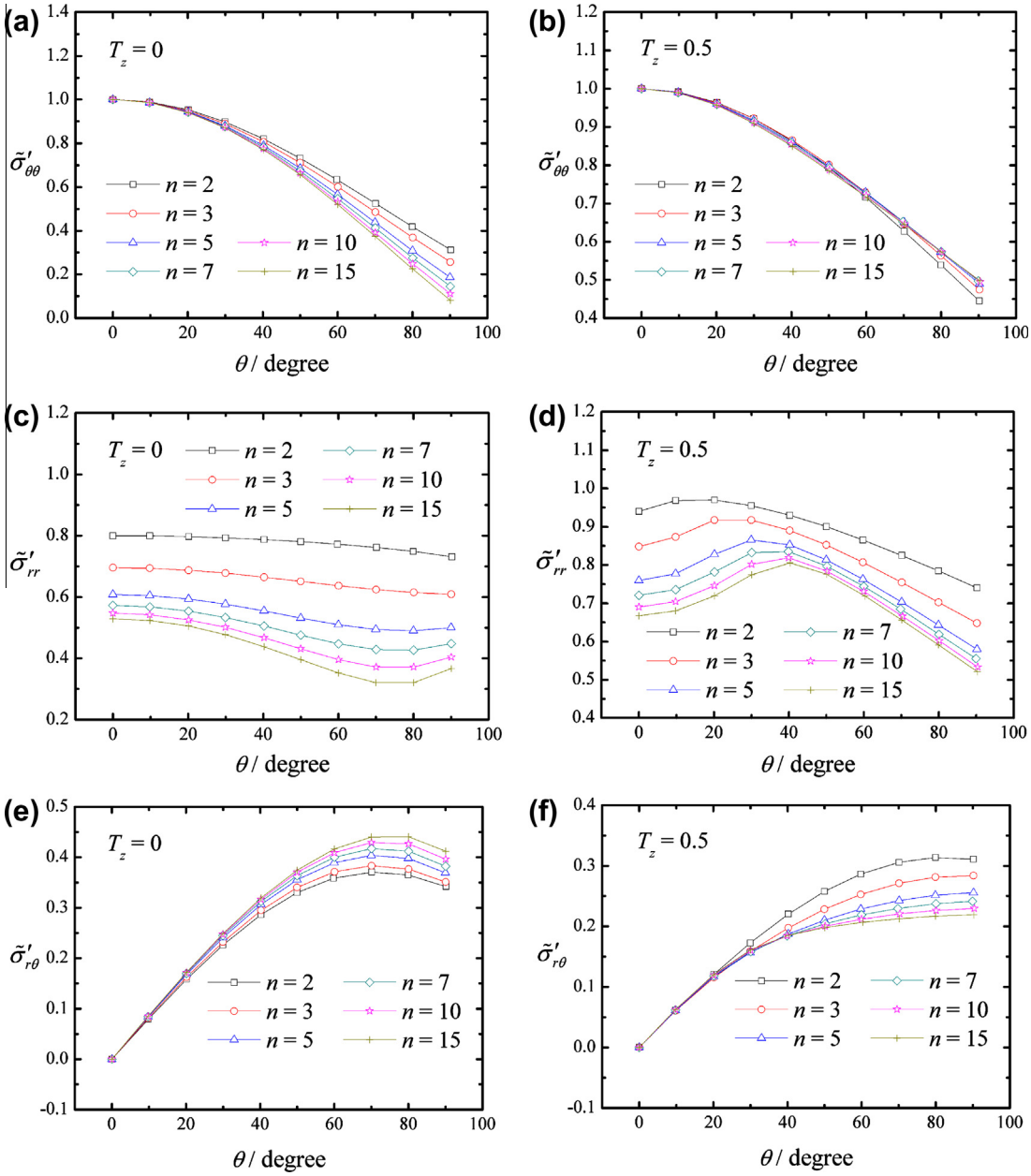

Fig. 4. Analytical results of $\tilde{\sigma}'_{ij}(n,\theta,0)$ and $\tilde{\sigma}'_{ij}(n,\theta,0.5)$ for different n plotted versus θ. (a) $\tilde{\sigma}'_{\theta\theta}(n,\theta,0)$; (b) $\tilde{\sigma}'_{\theta\theta}(n,\theta,0.5)$; (c) $\tilde{\sigma}'_{rr}(n,\theta,0)$; (d) $\tilde{\sigma}'_{rr}(n,\theta,0.5)$; (e) $\tilde{\sigma}'_{r\theta}(n,\theta,0)$; (f) $\tilde{\sigma}'_{r\theta}(n,\theta,0.5)$.

$$
\begin{aligned}
a &= (I_{0.5} + 10I_{0.3} + 5I_{0.1} - 5I_{0.4} - 10I_{0.2} - I_0)/0.0012,\\
b &= (I_{0.4} + 6I_{0.2} + I_0 - 4I_{0.3} - 4I_{0.1} - 0.0024a)/0.0024,\\
c &= (I_{0.3} + 3I_{0.1} - 3I_{0.2} - I_0 - 0.0015a - 0.0036b)/0.006,\\
d &= (I_{0.2} + I_0 - 2I_{0.1} - 0.0003a - 0.0014b - 0.006c)/0.02,\\
e &= (I_{0.1} - I_0 - 0.00001a - 0.0001b - 0.001c - 0.01d)/0.1,\\
f &= I_0.
\end{aligned}
$$

While for $n > 10$, we only need to translate the curve $[I_s(T_z,10)]^{1/(10+1)}$ from $(0,[I_s(0,10)]^{1/(10+1)})$ to $(0,[I_s(0,n)]^{1/(n+1)})$, that is

$$
[I_s(T_z,n)]^{1/(n+1)} = [I_s(T_z,10)]^{1/(10+1)} + [I_s(0,n)]^{1/(n+1)} - [I_s(0,10)]^{1/(10+1)}, \quad (n>10). \tag{2.6}
$$

Fig. 3 presents a comparison of the fitted variation of $[I_s(T_z,n)]^{1/(n+1)}$ with T_z for $n = 5$ and 15 against the analytical results. Good agreement can be seen.

In view of the relation between $[I_s(T_z,n)]^{1/(n+1)}$ and n, the analytical results of $[I_s(0,n)]^{1/(n+1)}$, $[I_s(0.1,n)]^{1/(n+1)}$, $[I_s(0.2,n)]^{1/(n+1)}$, $[I_s(0.3,n)]^{1/(n+1)}$, $[I_s(0.4,n)]^{1/(n+1)}$ and $[I_s(0.5,n)]^{1/(n+1)}$ varying with n is fitted in Appendix A.

2.2. Formulation of $\tilde{\sigma}'_{ij}(n,\theta,T_z)$ ($|\theta| \leqslant 90^\circ$)

The theoretical solutions of $\tilde{\sigma}'_{ij}(n,\theta,T_z)$ are too complicated to be expressed by a simple formula exactly, but a linear relation between $\tilde{\sigma}'_{ij}(n,\theta,T_z)$ and T_z is found that can represent the 3D state of $\tilde{\sigma}_{ij}(n,\theta,T_z)$ in the whole forward sector $|\theta| \leqslant 90^\circ$, which will be verified in Section 4. Then the relations between $\tilde{\sigma}'_{ij}(n,\theta,T_z)$ and θ at $T_z = 0$ and 0.5 are investigated.

Based on the 3D theoretical solutions by Guo (1993a, 1993b) and Xiang et al. (2011), the analytical results of the in-plane stresses $\tilde{\sigma}'_{\theta\theta}(n,\theta,T_z)$ plotted versus θ for different n at $T_z = 0$ and 0.5, at which the 3D solutions degrades to the plane stress and plane

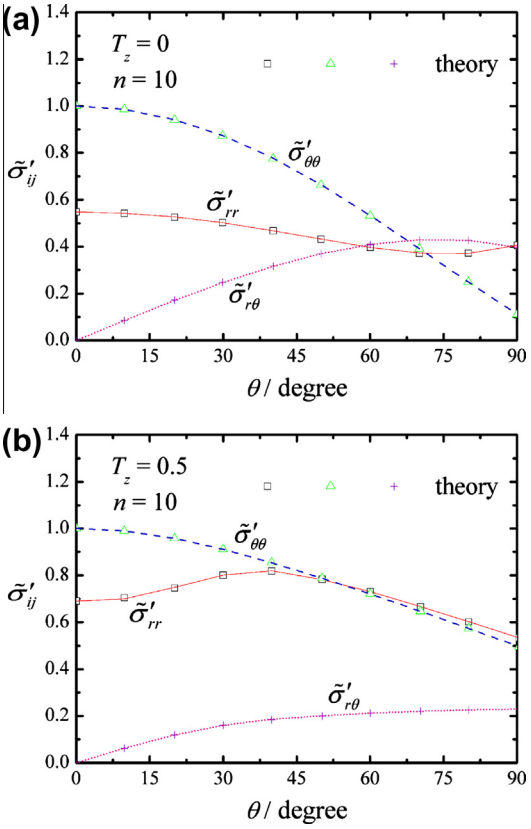

Fig. 5. (a) $\tilde{\sigma}'_{ij}(10,\theta,0)$ and (b)$\tilde{\sigma}'_{ij}(10,\theta,0.5)$ plotted versus θ.

strain HRR solution and the RR solution, respectively, can be obtained in the forward sector as shown in Fig. 4.

The angular distribution of $\tilde{\sigma}'_{ij}(n,\theta)$ at $T_z = 0$ for $\tilde{\sigma}'_{ij}(n,\theta,0)$ and $T_z = 0.5$ for $\tilde{\sigma}'_{ij}(n,\theta,0.5)$ presented in Fig. 4 can be fitted by two cubic curves expressed as

$$\tilde{\sigma}'_{ij}(n,\theta) = a\theta^3 + b\theta^2 + c\theta + d. \tag{2.7}$$

For $0^\circ \leqslant \theta \leqslant 45^\circ$,

$$a = [3\tilde{\sigma}'_{ij}(n,15^\circ) - \tilde{\sigma}'_{ij}(n,0^\circ) - 3\tilde{\sigma}'_{ij}(n,30^\circ) + \tilde{\sigma}'_{ij}(n,45^\circ)]/20,250,$$
$$b = [2\tilde{\sigma}'_{ij}(n,0^\circ) - 5\tilde{\sigma}'_{ij}(n,15^\circ) + 4\tilde{\sigma}'_{ij}(n,30^\circ) - \tilde{\sigma}'_{ij}(n,45^\circ)]/450,$$
$$c = [18\tilde{\sigma}'_{ij}(n,15^\circ) - 11\tilde{\sigma}'_{ij}(n,0^\circ) - 9\tilde{\sigma}'_{ij}(n,30^\circ) + 2\tilde{\sigma}'_{ij}(n,45^\circ)]/90,$$
$$d = \tilde{\sigma}'_{ij}(n,0^\circ).$$

For $45^\circ < \theta \leqslant 90^\circ$,

$$a = [3\tilde{\sigma}'_{ij}(n,60^\circ) - \tilde{\sigma}'_{ij}(n,45^\circ) - 3\tilde{\sigma}'_{ij}(n,75^\circ) + \tilde{\sigma}'_{ij}(n,90^\circ)]/20,250,$$
$$b = [5\tilde{\sigma}'_{ij}(n,45^\circ) - 14\tilde{\sigma}'_{ij}(n,60^\circ) + 13\tilde{\sigma}'_{ij}(n,75^\circ) - 4\tilde{\sigma}'_{ij}(n,90^\circ)]/450,$$
$$c = [189\tilde{\sigma}'_{ij}(n,60^\circ) - 74\tilde{\sigma}'_{ij}(n,45^\circ) - 162\tilde{\sigma}'_{ij}(n,75^\circ) + 47\tilde{\sigma}'_{ij}(n,90^\circ)]/90,$$
$$d = 20\tilde{\sigma}'_{ij}(n,45^\circ) - 45\tilde{\sigma}'_{ij}(n,60^\circ) + 36\tilde{\sigma}'_{ij}(n,75^\circ) - 10\tilde{\sigma}'_{ij}(n,90^\circ),$$

where, the $\tilde{\sigma}'_{\theta\theta}(n,\theta)$, $\tilde{\sigma}'_{rr}(n,\theta)$ and $\tilde{\sigma}'_{r\theta}(n,\theta)$ at 0°, 15°, 30°, 45°, 60°, 75° and 90° can be easily obtained from the formulae of $\tilde{\sigma}_{ij}(n,\theta)$ varying with n at these angles, as presented in Appendices B, C and D, respectively.

Then the formulation of $\tilde{\sigma}'_{ij}(n,\theta,T_z) = \frac{\tilde{\sigma}_{ij}(n,\theta,T_z)}{\tilde{\sigma}_{\theta\theta}(n,0,T_z)}$ in the whole forward sector $|\theta| \leqslant 90^\circ$ empirically can be obtained as

$$\tilde{\sigma}'_{ij}(n,\theta,T_z) = 2T_z[\tilde{\sigma}'_{ij}(n,\theta,0.5) - \tilde{\sigma}'_{ij}(n,\theta,0)] + \tilde{\sigma}'_{ij}(n,\theta,0). \tag{2.8}$$

Fig. 5 presents the angular variation of $\tilde{\sigma}'_{ij}(n,\theta,T_z)$ for $n = 10$ at $T_z = 0$ and $T_z = 0.5$. It is convinced that the obtained empirical formulae (shown as lines) can well represent the analytical results (shown as data points).

With $[I_s(T_z,n)]^{1/(n+1)}$ and $\tilde{\sigma}'_{ij}(n,\theta,T_z)$ being formulized, we can then easily obtain the formulation of σ_{ij} in the sector of $|\theta| \leqslant 90^\circ$ by Eqs. (2.1)–(2.4).

2.3. Stress triaxiality R_σ

The stress triaxiality which dominates ductile fracture is defined as follows:

$$R_\sigma = \sigma_m/\sigma_e, \tag{2.9}$$

where σ_m is the hydrostatic stress and σ_e is the Von Mises equivalent stress,

$$\sigma_m = \frac{1}{3}(1+T_z)(\sigma_{rr} + \sigma_{\theta\theta}), \tag{2.10}$$

$$\sigma_e = [(1 - T_z + T_z^2)(\sigma_{rr}^2 + \sigma_{\theta\theta}^2) - (1 + 2T_z - 2T_z^2)\sigma_{rr}\sigma_{\theta\theta} + 3(\sigma_{r\theta}^2 + \sigma_{rz}^2 + \sigma_{\theta z}^2)]^{1/2}. \tag{2.11}$$

As shown in (Guo, 1993a; Xiang et al., 2011), for 3D mode-I crack problems under power law plastic and creeping conditions, σ_{rz} and $\sigma_{\theta z}$ can be neglected in the vicinity of crack tip. Furthermore, $\sigma_{r\theta}$ on the ligament ahead of the crack border is zero due to the symmetry requirement. Then σ_e on the ligament can be reduced to

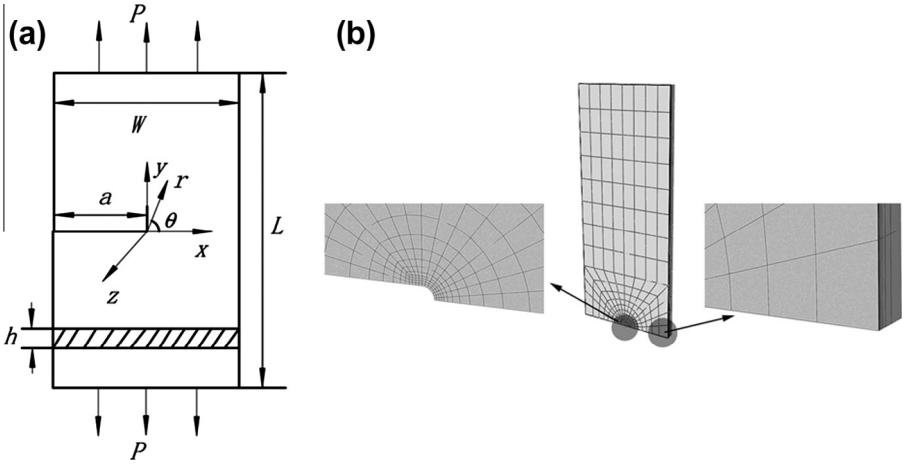

Fig. 6. (a) Schematic of the SEC specimen subjected to symmetrical remote loading; (b) Finite element mesh for upper half, crack-tip region and half-thickness.

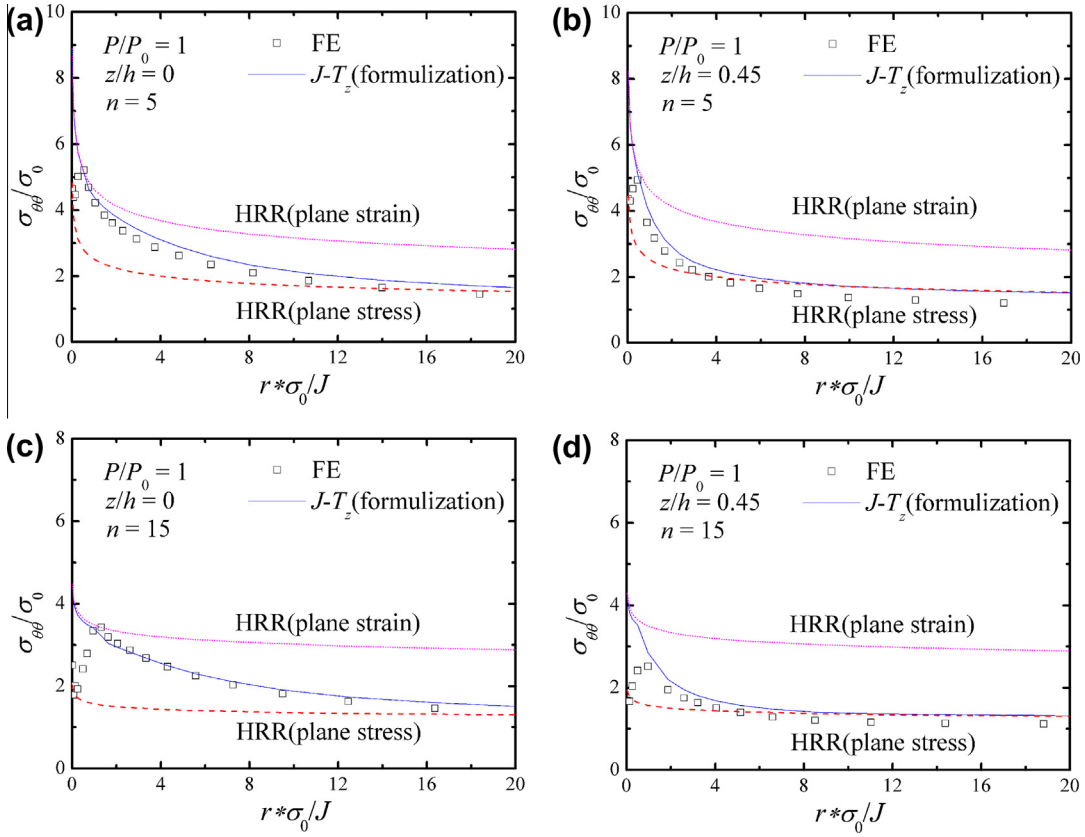

Fig. 7. Comparisons of $\sigma_{\theta\theta}$ obtained by the formulation of J–T_z solution with the 3D FE results, and HRR solutions. (a) $n_1 = 5$, $z/h = 0$; (b) $n_1 = 5$, $z/h = 0.45$; (c) $n_1 = 15$, $z/h = 0$; (d) $n_1 = 15$, $z/h = 0.45$.

$$\sigma_e = [(1 - T_z + T_z^2)(\sigma_{rr}^2 + \sigma_{\theta\theta}^2) - (1 + 2T_z - 2T_z^2)\sigma_{rr}\sigma_{\theta\theta}]^{1/2}, \quad \theta = 0. \tag{2.12}$$

Then R_σ on the ligament ahead of the crack border can be reduced to

$$R_\sigma = \frac{\frac{1}{3}(1 + T_z)(\sigma_{rr} + \sigma_{\theta\theta})}{[(1 - T_z + T_z^2)(\sigma_{rr}^2 + \sigma_{\theta\theta}^2) - (1 + 2T_z - 2T_z^2)\sigma_{rr}\sigma_{\theta\theta}]^{1/2}}, \quad \theta = 0. \tag{2.13}$$

3. Numerical model

To verify the efficiency of the asymptotic solution, ABAQUS 6.8 is employed to model the cases of single-edge cracked (SEC) specimens under mode I condition as shown in Fig. 6(a). The dimensions of the specimens are as follows: $W = 25.4$ mm, $L = 114.3$ mm, thickness $h = 4$ mm, $a/W = 0.5$. For the SEC specimens, the crack length are designated a and the total width as W as usual. Only a quarter of the plate is modeled with finite elements, since the problem has reflective symmetry with respect to the mid-plane ($z = 0$) and the crack ligament plane ($y = 0$). The finite element mesh is constructed with 20-node 3D brick elements. In the plane (x–y plane) perpendicular to the crack front, the element size gradually increases with increasing radial distance from the crack tip, while there are 16 elements in each circular ring surrounding the crack tip. To consider the detail of large deformation and blunting of the crack tip, an initial notches with root radius $\rho = 0.001$ mm is adopted (Graba and Galkiewicz, 2007), as shown in Fig. 6(b). The identical planar mesh is repeated along the z-axis from the symmetry-plane ($z = 0$) to the free surface ($z/h = 0.5$). In order to accommodate the strong variations of field quantities with respect to the z-axis, the thickness of successive element layers is gradually reduced toward the free surface. There are 10 element layers through the half-thickness, and each layer contains 656 elements.

The material constitutive model is given by Eqs. (1.2) and (1.5):

For power law plastic solids, $n_1 = 5, 15$, $E = 206$ GPa, $\nu = 0.3$, $\alpha = 1$, $\sigma_0 = 500$ MPa, and $\varepsilon_0 = \sigma_0/E = 0.00243$. The specimen is subjected to a constant remote tensile stress, $P/P_0 = 1$, where P_0 is the plane stress limit load for a rigid perfectly plastic material. For the SEC specimen configuration considered in this paper, $P_0 = 1.072\eta c\sigma_0$, where η is defined as $\eta = [1 + (a/c)^2]^{1/2} - a/c$ and $c = W - a$.

For power law creeping solids, $n_2 = 10$, $E = 154$ GPa, $\nu = 0.33$, $B = 2 \times 10^{-90}\,(\text{Pa})^{-n2}/\text{h}$, $\sigma_0 = 417$ MPa, and $\dot{\varepsilon}_0 = B\sigma_0^{n_2} = 3.18 \times 10^{-4}\ \text{h}^{-1}$. The specimen is subjected to a constant remote tensile stress for all time ($t = 0 \to \infty$), $P = 0.54P_0 = 5080N$.

4. Result analyses

4.1. Result analyses in power law plastic solids ($\theta = 0°$)

Figs. 7–9 compare the distributions of $\sigma_{\theta\theta}$, σ_{rr} and R_σ for $n_1 = 5$, 15, $P/P_0 = 1$ and $z/h = 0$, 0.45 obtained by the formulized J–T_z solutions with the 3D finite element results. HRR-type solutions (plane stress and plane strain) are also included in the comparison to demonstrate the inadequacy of 2D solution in predicting the 3D stress fields near the crack border in finite thickness plates. In the figures, all the stresses on the ordinate are normalized by the yield strength σ_0, and all the distances on the abscissa are normalized by J/σ_0.

4.1.1. Results of $\sigma_{\theta\theta}$ and σ_{rr} ($\theta = 0°$)

Comparisons in Figs. 7 and 8 show that the formulized solutions can well predict the distributions of $\sigma_{\theta\theta}$ and σ_{rr} in the range of

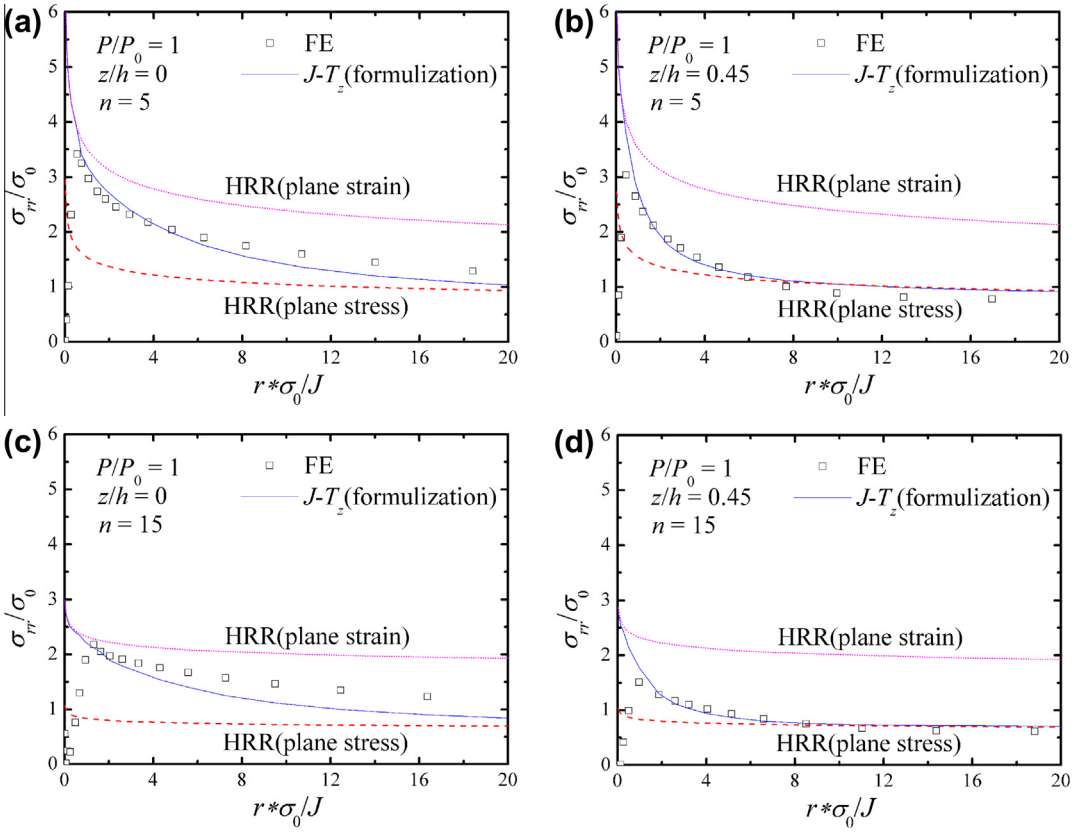

Fig. 8. Comparisons of σ_{rr} obtained by the formulation of J–T_z solution with the 3D FE results, and HRR solutions. (a) $n_1 = 5$, $z/h = 0$; (b) $n_1 = 5$, $z/h = 0.45$; (c) $n_1 = 15$, $z/h = 0$; (d) $n_1 = 15$, $z/h = 0.45$.

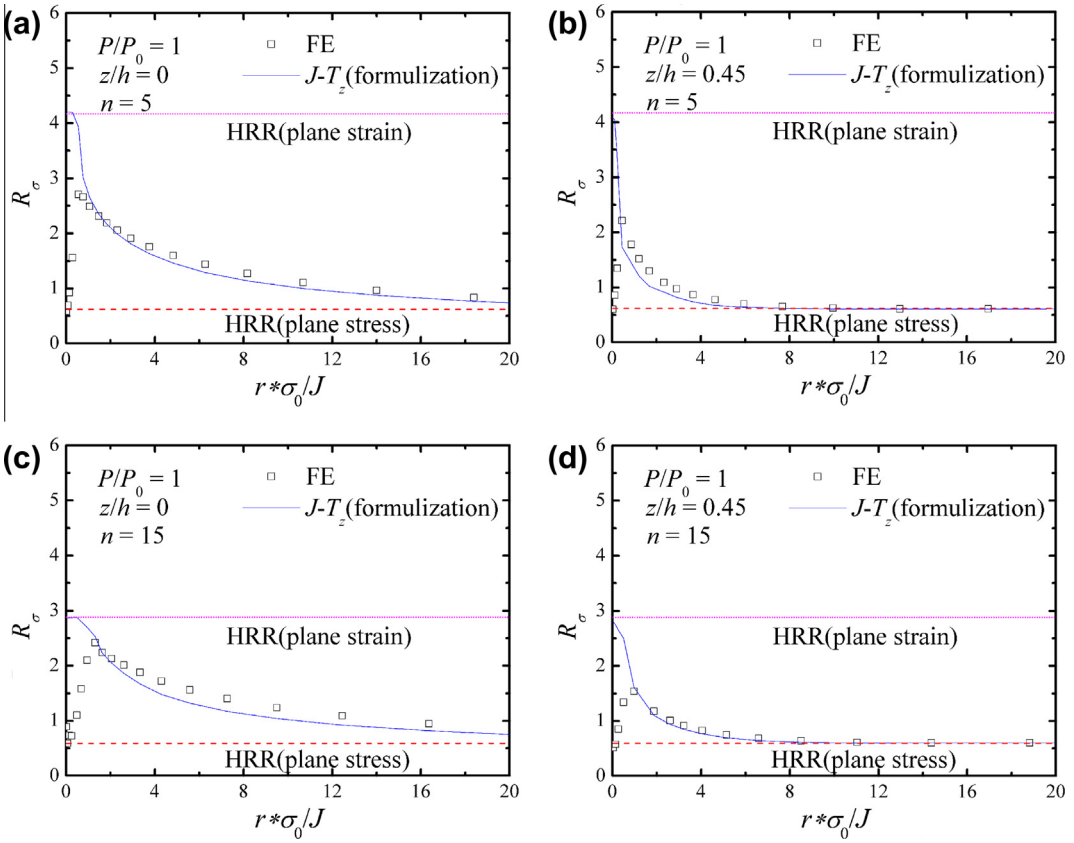

Fig. 9. Comparisons of R_σ obtained by the formulation of J–T_z solution with the 3D FE results, and HRR solutions. (a) $n_1 = 5$, $z/h = 0$; (b) $n_1 = 5$, $z/h = 0.45$; (c) $n_1 = 15$, $z/h = 0$; (d) $n_1 = 15$, $z/h = 0.45$.

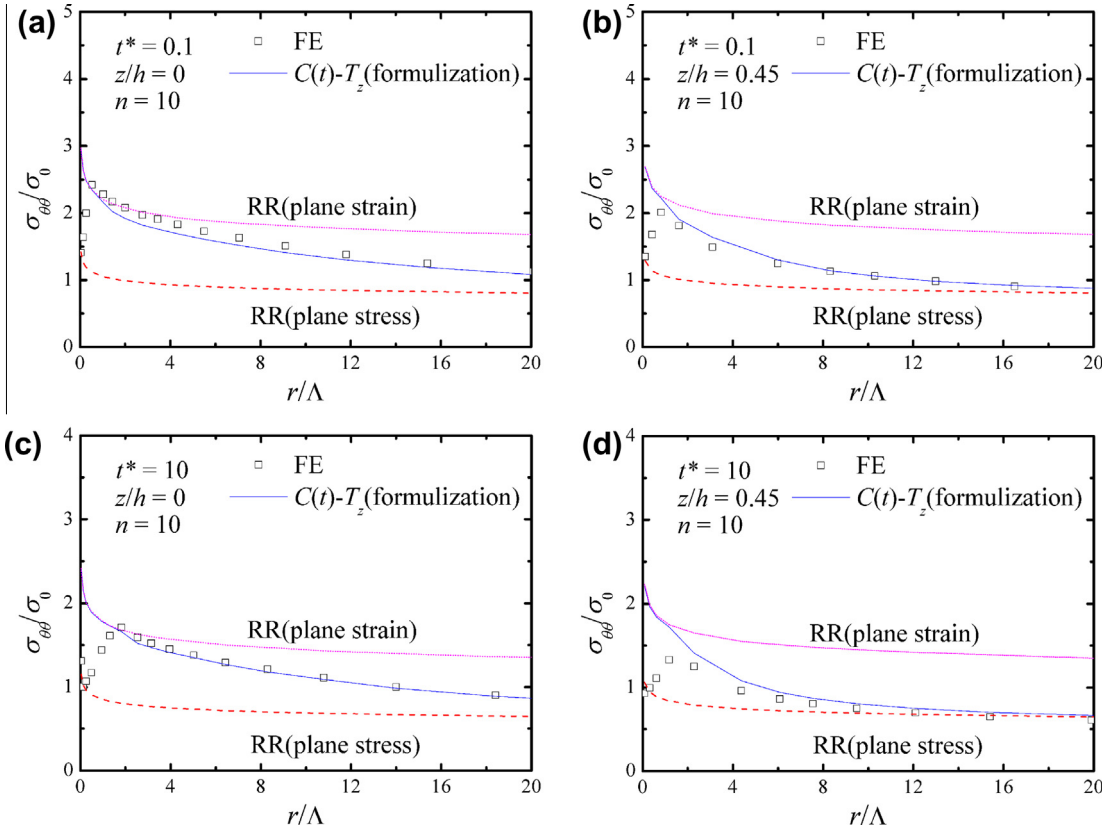

Fig. 10. Comparisons of $\sigma_{\theta\theta}$ obtained by the formulation of $C(t)$–T_z solution with the 3D FE results and RR solutions. (a) $t^* = 0.1$, $z/h = 0$; (b) $t^* = 0.1$, $z/h = 0.45$; (c) $t^* = 10$, $z/h = 0$; (d) $t^* = 10$, $z/h = 0.45$.

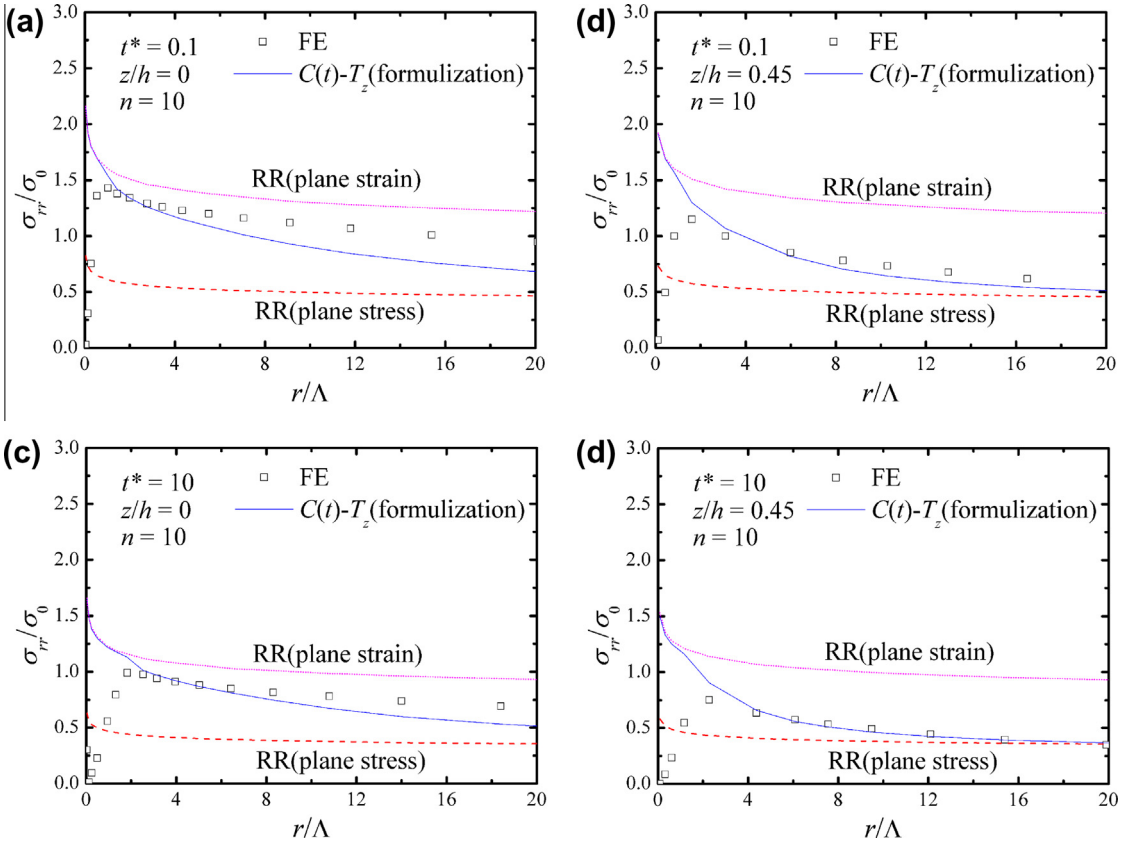

Fig. 11. Comparisons of σ_{rr} obtained by the formulation of $C(t)$–T_z solution with the 3D FE results and RR solutions. (a) $t^* = 0.1$, $z/h = 0$; (b) $t^* = 0.1$, $z/h = 0.45$; (c) $t^* = 10$, $z/h = 0$; (d) $t^* = 10$, $z/h = 0.45$.

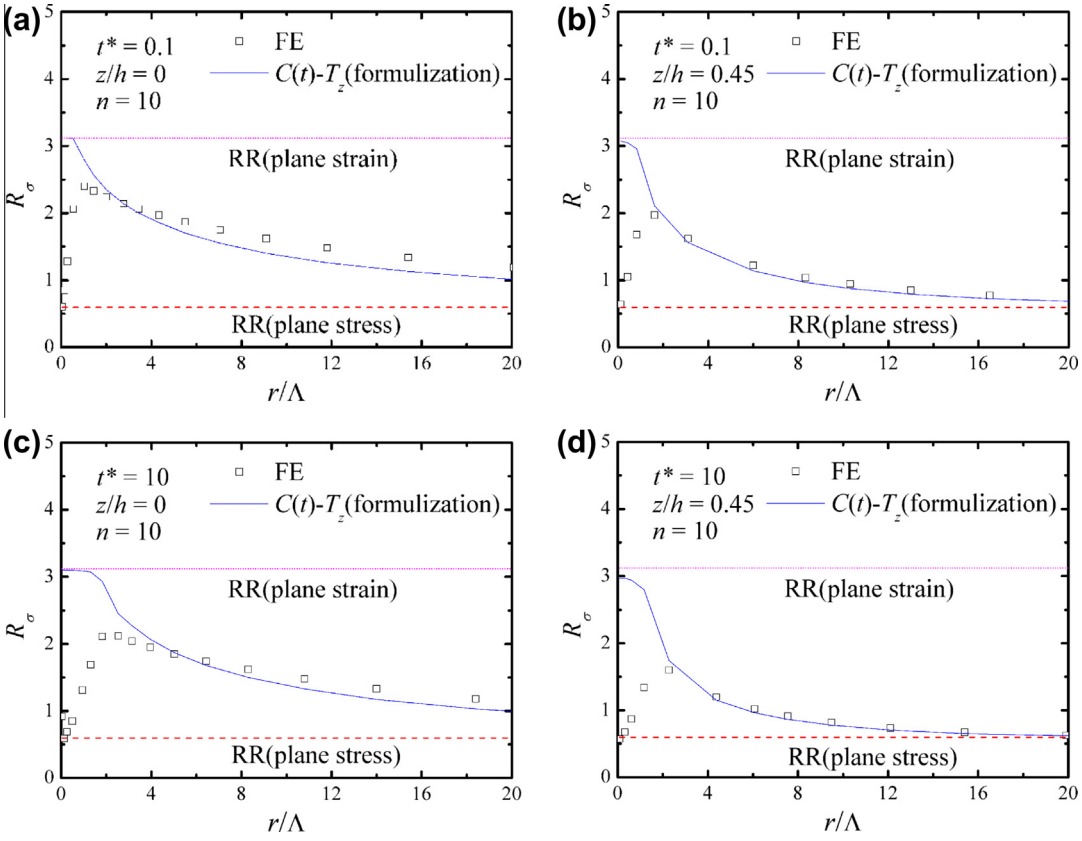

Fig. 12. Comparisons of R_σ obtained by the formulation of $C(t)$–T_z solution with the 3D FE results and RR solutions. (a) $t^* = 0.1$, $z/h = 0$; (b) $t^* = 0.1$, $z/h = 0.45$; (c) $t^* = 10$, $z/h = 0$; (d) $t^* = 10$, $z/h = 0.45$.

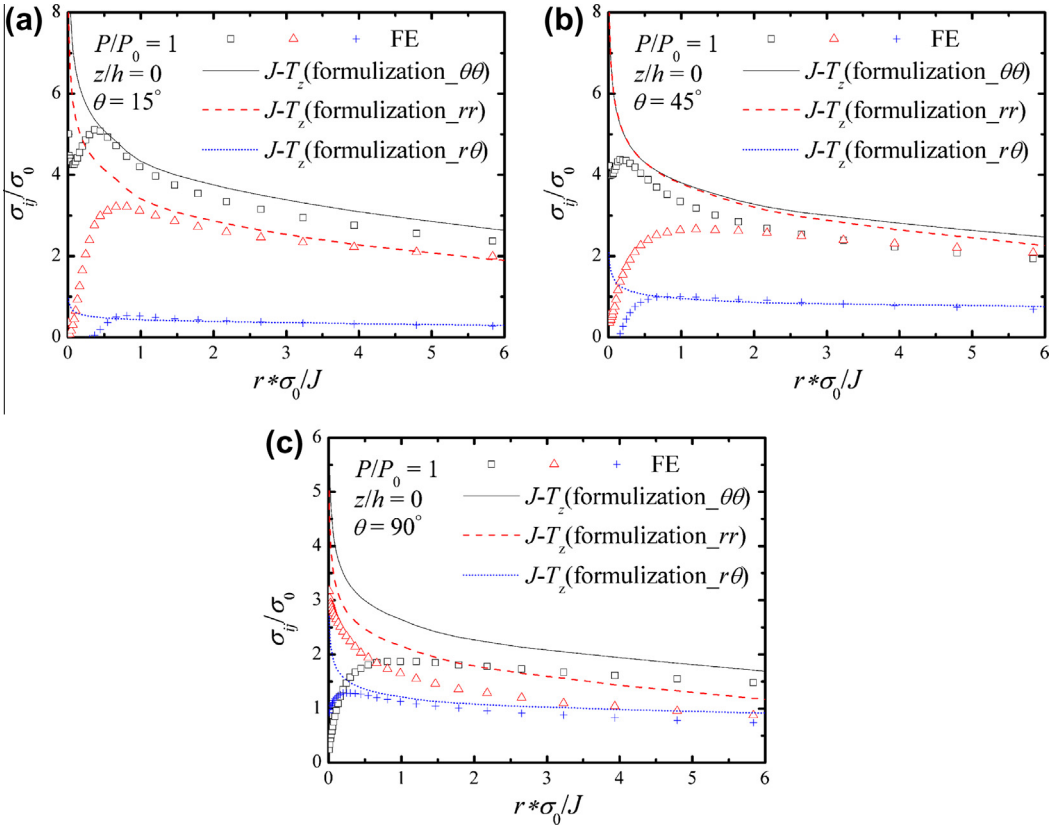

Fig. 13. Comparisons of the stress components obtained by the formulation of J–T_z solution with 3D FE results at (a) $\theta = 15°$; (b) $\theta = 45°$; (c) $\theta = 90°$.

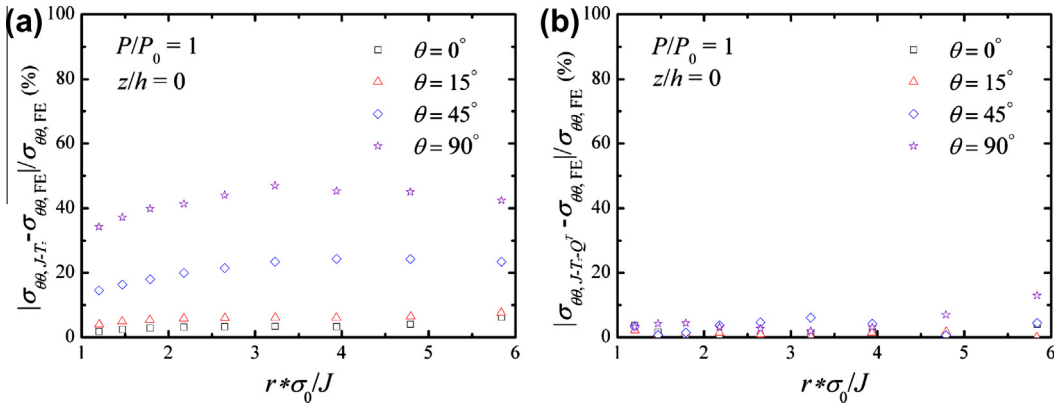

Fig. 14. The percentage errors with respect to the numerical results for (a) J–T_z description and (b) J–T_z–Q^T description for SEC specimens at different angles.

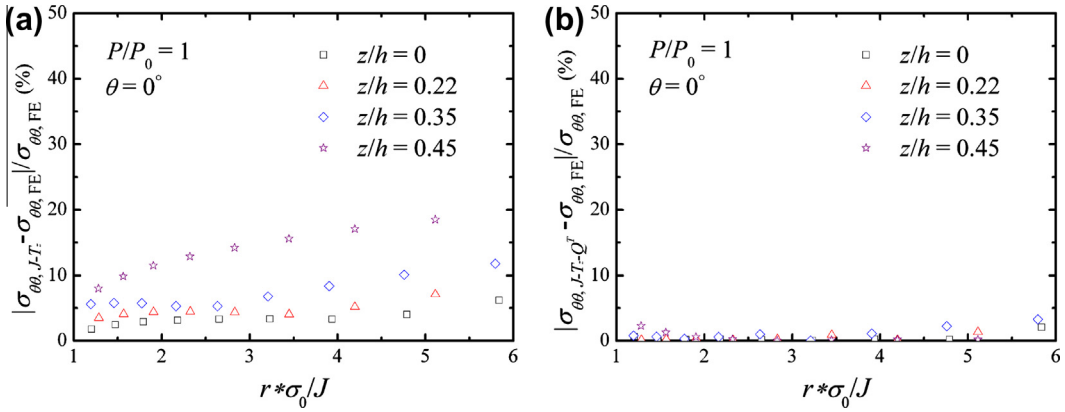

Fig. 15. The percentage errors with respect to the numerical results for (a) J–T_z description and (b) J–T_z–Q^T description for SEC specimens along the thickness of the plate.

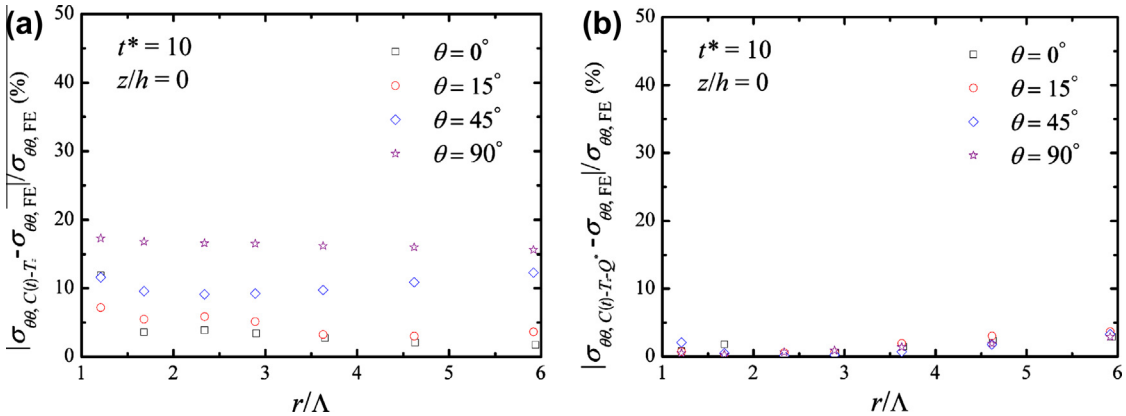

Fig. 16. The percentage errors with respect to the numerical results for (a) $C(t)$–T_z description and (b) $C(t)$–T_z–Q^* description for SEC specimens at different angles.

interest, which is suggested to be within the range of $1 < r/(J/\sigma_0) < 5$ (Ritchie et al., 1973; Ritchie and Thompson, 1985), and are much closer to the finite element results than the HRR solution over a wide crack border region, thus representing the actual 3D states of $\sigma_{\theta\theta}$ and σ_{rr} are transition states from HRR solutions of plane strain state near the crack tip to HRR solutions of plane stress state far from the crack tip in the interior of the plate from $z/h = 0$ to 0.45.

4.1.2. Results for R_σ ($\theta = 0°$)

As $\sigma_{\theta\theta}$ and σ_{rr} can be well predicted by the formulized solutions, then the formulized predictions for R_σ can be obtained from (2.13). Fig. 9 shows that R_σ on the ligament ahead of the crack can be well predicted by the formulized solutions too, and the 3D state of R_σ shows a transition from HRR solution of plane strain state to HRR solution of plane stress state with distance increasing from the crack tip, obviously.

4.2. Result analyses in power law creeping solids ($\theta = 0°$)

We proceed to verify the formulation under power law creeping condition. Figs. 10–12 compare the distributions of $\sigma_{\theta\theta}$, σ_{rr} and R_σ for $n_2 = 10$, $z/h = 0$, 0.45 and $t^* = 0.1$, 10 obtained by the formulation of the $C(t)$–T_z solution with 3D finite element results. The RR-type solutions (plane stress and plane strain) are also included in the comparison. Where $t^* = t/t_T$, and t_T is the transition time, $t_T = J/[(n+1)C^*]$. All the all the stresses on the ordinate are normalized by the initial yield strength σ_0, and all the distances on the abscissa are normalized by Λ (Xiang et al., 2011), which is analogous to J/σ_0 in power law plastic solids, as follows

$$\Lambda = r\sigma_0/[C(t)t(n+1)^{(n+1)/n}\tilde{t}^{1/n}], \quad (t^* \ll 1 \text{ or small scale creep}),$$

$$\Lambda = r\sigma_0/(C^* t\tilde{t}^{1/n}), \quad (t^* \gg 1 \text{ or extensive creep}),$$

where $\tilde{t}$ is dimensionless quantity extracted from t.

4.2.1. Results of $\sigma_{\theta\theta}$ and σ_{rr} ($\theta = 0°$)

Under both small scale and extensive creep conditions, Figs. 10 and 11 show that the $C(t)$–T_z formulation of $\sigma_{\theta\theta}$ and σ_{rr} can provide excellent prediction in the range of interest, $1 < r/\Lambda < 5$, and are much closer to the finite element results than the RR solutions in a large region. The actual 3D distributions of $\sigma_{\theta\theta}$ and σ_{rr} in power law creeping solids take a trend to shift from the plane strain RR solution near the crack tip to plane stress RR solution far from the crack tip, similar to that in power law plastic solids.

4.2.2. Results for R_σ ($\theta = 0°$)

Based on the formulations of $\sigma_{\theta\theta}$ and σ_{rr} in creeping solids, R_σ can be obtained simply from (2.13) on the ligament. As shown by the comparisons in Fig. 12, the formulized solutions can provide an excellent prediction of the 3D distributions of R_σ, which have the similar transition trend from the plane strain RR solution near the crack tip to the plane stress RR solution far away from the crack tip.

4.3. Results of stress components in power law plastic solids ($0° < \theta \leqslant 90$)

Here, the distributions of σ_{ij} in power law plastic solids are considered in the mid-plane only, and the analogy between power law creeping and power law plasticity suggests that it will be the same case in power law creeping solids. Fig. 13 compares the distributions of σ_{ij} for $n_1 = 5$, $P/P_0 = 1$ and $\theta = 15°$, 45°, 90° obtained by 3D finite element analyses and the empirically formulized J–T_z solutions. All the ordinates are normalized by the yield strength σ_0, and all the abscissas are normalized by J/σ_0. From the figure it can be seen that $\sigma_{\theta\theta}$ and σ_{rr} can only be well predicted for relatively small crack border angles θ ($|\theta| \leqslant 15°$), while $\sigma_{r\theta}$ can be excellently predicted by the proposed formulation almost in the whole forward sector $|\theta| \leqslant 90°$. For larger θ ($|\theta| \geqslant 45°$), similar as apparent in-plane constraint lost shown by the J–Q solution (O'dowd and Shih, 1991, 1992), the empirically formulated J–T_z solution has larger deviation from the finite element results.

5. Three-parameter descriptions

Based on the formulation, we proceed to compare the percentage errors with respect to the 3D finite element results between the J–T_z description and J–T_z–Q^T description (Guo, 2000) for plastic solids and between the $C(t)$–T_z description and $C(t)$–T_z–Q^* description (Xiang et al., 2011) for creeping solids.

For small scale yield and creep conditions, the in-plane constraint lost described by parameters Q^T and Q^* will be limited by the surrounding elastic fields, especially on the ligament directly ahead of the cracks. Here we choose the power law plastic solids under high load of $P/P_0 = 1$ and power law creeping solids at extensive creeping duration $t^* = 10$ to discuss the necessity of three-parameter descriptions under large scale yielding conditions. The discussion is limited to the distributions of $\sigma_{\theta\theta}$ in the forward sector of the cracks for simplicity.

5.1. Result analyses in power law plastic solids

Guo (2000) has proposed the J–T_z–Q^T description under large scale yielding plastic deformation as follows

$$\sigma_{ij} = \sigma_0\left[\frac{J}{\alpha\varepsilon_0\sigma_0 I(T_z, n_1)r}\right]^{\frac{1}{n_1+1}}\tilde{\sigma}_{ij}(n_1, \theta, T_z) + Q^T\sigma_0\delta_{ij}, \tag{5.1}$$

where

$$Q^T = \frac{(\sigma_{ij})_{FE} - (\sigma_{ij})_{J-T_z}}{\sigma_0} \quad \text{at } r = 2J/\sigma_0. \tag{5.2}$$

Figs. 14 and 15 show the percentage errors of $\sigma_{\theta\theta}$ for $n_1 = 5$ for different angles and along the thickness of the plate. Obviously, the J–T_z–Q^T description is much better than the J–T_z description.

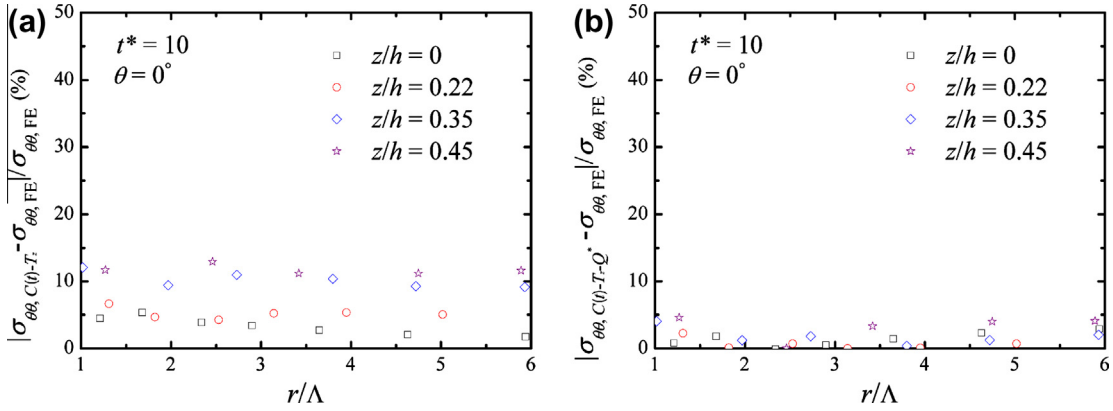

Fig. 17. The percentage errors with respect to the numerical results for (a) $C(t)$–T_z description and (b) $C(t)$–T_z–Q^* description for SEC specimens along the thickness of the plate.

5.2. Result analyses in power law creeping solids

Xiang et al. (2011) has proposed the following $C(t)$–T_z–Q^* description to consider both the in-plane and out-of-plane constraints.

$$\sigma_{ij} = \sigma_0 \left[\frac{C(t)}{\sigma_0 \dot{\varepsilon}_0 I(T_z, n) r}\right]^{\frac{1}{n+1}} \tilde{\sigma}_{ij}(\theta, T_z) + Q^* \sigma_0 \delta_{ij}, \tag{5.3}$$

where

$$Q^* = \frac{(\sigma_{ij})_{FE} - (\sigma_{ij})_{C(t)-T_z}}{\sigma_0} \quad \text{at } r = 2\Lambda. \tag{5.4}$$

Figs. 16 and 17 show the percentage errors of $\sigma_{\theta\theta}$ for $n_2 = 10$ at different angles and along the thickness of the plate. It can be seen that the $C(t)$–T_z–Q^T description is much more efficient than the $C(t)$–T_z description.

For single-edge cracked specimens which develop full constrained crack border fields, three-parameter description, J–T_z–Q^T description or $C(t)$–T_z–Q^* description, is even necessary to be introduced under large scale yield and extensive creep conditions, not to mention the specimens which develop unconstrained crack tip fields, such as center-cracked tension specimens discussed by Xiang et al. (2011), additional constraint lost is required to take into account, even at $\theta = 0$ or $z/h = 0$.

It is important to note that the in-plane constraint lost in the whole forward sector of cracks ($|\theta| \leqslant 90^\circ$) can be efficiently described by the three-parameter systems in both power law plastic and creeping plates with finite thicknesses.

6. Discussion

For convenience of analysis, the discussion will be limited to the power law plastic conditions, and the analogy between power law creeping and power law plasticity suggests that it will be the same case in power law creeping conditions.

Guo (1995) had given the explicit form of T_z for a through-thickness crack subjected to mode I loading as follows:

$$T_z = \frac{1}{2}\left[1 - (1-2\nu)\left(\frac{r}{\overline{r_p}}\right)^{\frac{n-1}{2.3n+1}}\right] \times \left[1 - 1.218\left(\frac{r}{h}\right)^{0.5} - 0.359\left(\frac{r}{h}\right) + 0.361\left(\frac{r}{h}\right)^{1.5}\right]\left[1 - \left|\frac{2z}{h}\right|^{0.94\left(\frac{r}{h}\right)^{-0.58}}\right]^2, \tag{6.1}$$

where $\overline{r_p}$ is the average size of plastic zone through the thickness of the plate.

Under small-scale yielding (SSY) condition, it has been shown by Guo (1995) that $\overline{r_p}$ can be predicted by

$$\overline{r_p} = \frac{\pi}{8}\frac{n}{n+1}\frac{1}{\alpha^2}\frac{J^{far}}{\sigma_0 \varepsilon_0}, \quad (\theta = 0), \tag{6.2}$$

$$\alpha = \frac{1 + \overline{r_{p0}}/h}{1 + \overline{r_{p0}}/h - 2\nu}, \tag{6.3}$$

where $\overline{r_{p0}} = \overline{r_p}|_{\alpha=1}$.

For load levels greater than $J^{far}/\sigma_0 \varepsilon_0 h \approx 5$, Nakamura and Parks (1990) found that the maximum in-plane extent of plastic zone can be approximated as

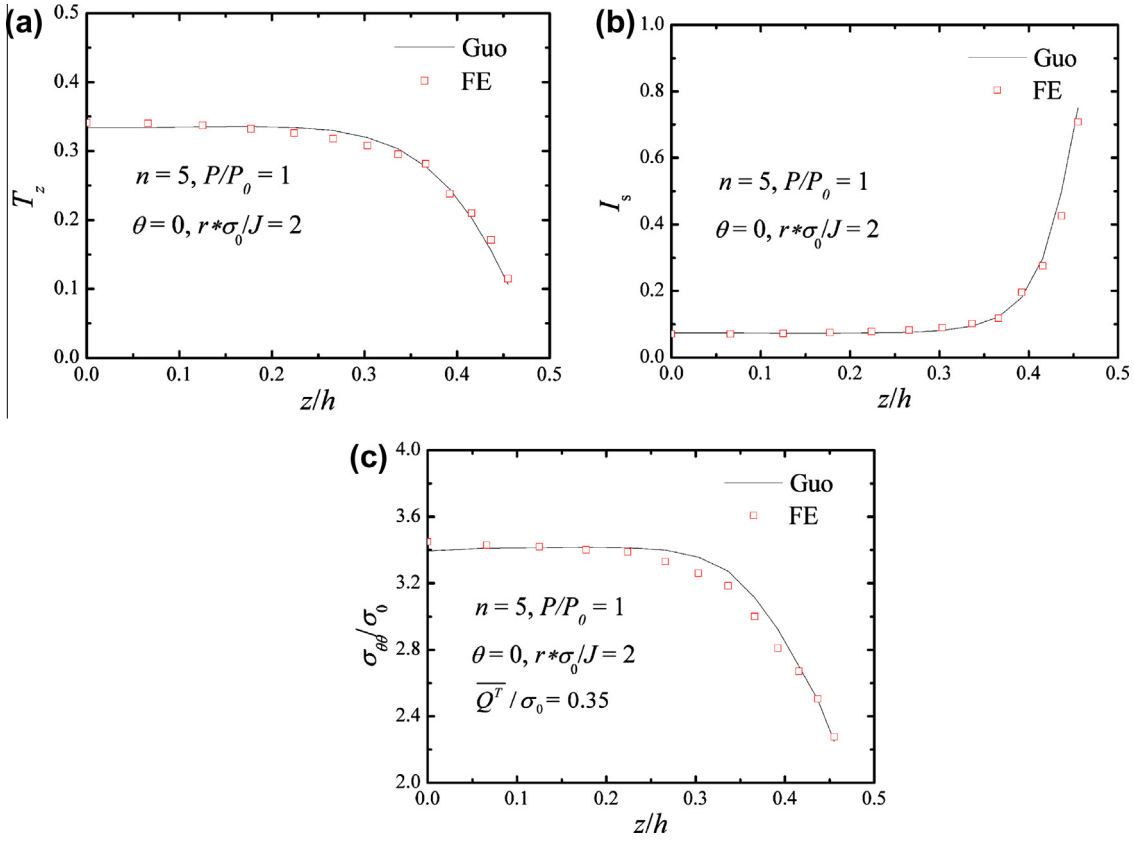

Fig. 18. Comparisons of (a) T_z, (b) I_s, (c) $\sigma_{\theta\theta}$ from $z/h = 0$ to $z/h = 0.5$ obtained by the 3D FE result and prediction based on Guo's fitting solution.

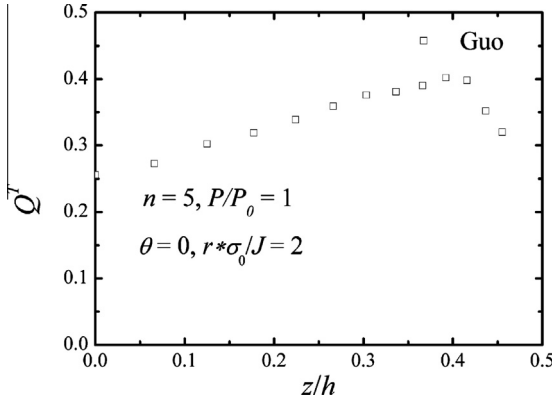

Fig. 19. Distribution of Q^T from $z/h = 0$ to $z/h = 0.5$ based on Guo's fitting solution.

$$\frac{r_p}{J^{far}/\sigma_0\varepsilon_0 h} \approx 0.24, \quad (\theta = 0), \tag{6.4}$$

where r_p is the extent of the plastic zone directly ahead of the crack front ($\theta = 0$).

Based on the explicit form of T_z, I_s and $\sigma_{\theta\theta}$ can be obtained further. Fig. 18 presents the comparisons of T_z, I_s and $\sigma_{\theta\theta}$ between 3D FE result and prediction based on Guo's fitting solution at $r/(J/\sigma_0) = 2$ through the thickness from $z/h = 0$ to $z/h = 0.5$ for elastic–plastic crack problems with $n_1 = 5$. It is shown that T_z can be well predicted by Eq. (6.1), resulting in a wonderful prediction for I_s, which is only dependent on T_z for given materials. While it is necessary to introduce an in-plane constraint lost to predict $\sigma_{\theta\theta}$ as discussed in Section 5. In Fig. 18(c), a through-the-thickness average parameter of $\overline{Q^T}$ was introduced to make a satisfied prediction for the through thickness distribution of $\sigma_{\theta\theta}$ on the ligament at $r/(J/\sigma_0) = 2$ by using the predicted T_z and I_s. It is should be noted that using of (6.2), (6.4) leads to very close prediction to the through-the-thickness distributions of T_z, I_s and $\sigma_{\theta\theta}$ here.

When the in-plane constraint lost Q^T is evaluated by match the theoretical prediction and the finite element results for the SEC specimen, it is found that that Q^T increases with increasing z/h and approaches to its maximum in range of $z/h = 0.35$–0.4, and then decreases with further increasing z/h to the free surface, as shown in Fig. 19.

7. Conclusions

Based on a comprehensive understanding of the feature of stress fields ahead of 3D cracks, a set of empirical explicit formulae for the crack border stress fields is obtained by fitting the J–T_z theoretical solution by Guo (1993a, 1993b) for plastic solids obeying the power law of $\varepsilon = \alpha\varepsilon_0\left(\frac{\sigma}{\sigma_0}\right)^{n_1}$ as

$$\sigma_{ij} = \sigma_0\left[\frac{J}{\alpha\varepsilon_0\sigma_0 I_s(T_z, n_1)r}\right]^{\frac{1}{n_1+1}}\tilde{\sigma}'_{ij}(n_1, \theta, T_z), \quad (i,j = r, \theta);$$

and the $C(t)$–T_z solution by Xiang et al. (2011) for creeping solid obeying the power law of $\dot{\varepsilon} = \dot{\varepsilon}_0\left(\frac{\sigma}{\sigma_0}\right)^{n_2}$ as

$$\sigma_{ij} = \sigma_0\left[\frac{C(t)}{\dot{\varepsilon}_0\sigma_0 I_s(T_z, n_2)r}\right]^{\frac{1}{n_2+1}}\tilde{\sigma}'_{ij}(n_2, \theta, T_z), \quad (i,j = r, \theta).$$

Empirical formulae for $I_s(T_z, n)$ and $\tilde{\sigma}'_{ij}(n, \theta, T_z)$ were presented explicitly for $2 < n < 20$ in the forward sector of $|\theta| \leqslant 90^\circ$ as well as the out-of-plane stress constraint factor $T_z = \frac{\sigma_{33}}{\sigma_{11}+\sigma_{22}}$ in the whole range from $T_z = 0$ for plane stress state to $T_z = 0.5$ for plane strain state. At the limits of $T_z = 0$ and 0.5, the empirical formulae can degrade into explicit expression with high accuracy for the 2D HRR and RR solutions.

Detailed 3D finite element analyses have been performed for single-edge cracked specimens with finite thickness to verify the formulation. In small scale yielding and confined creeping conditions, the formulation for the J–T_z and $C(t)$–T_z solutions has been proven to be efficient to represent the distributions of in-plane stresses and stress triaxiality on the ligament directly ahead of the crack border in both of the plastic and creeping plates with finite thickness. Under large yielding/creeping conditions, the lost in in-plane stress constraint have to be considered and three-parameter descriptions of J–T_z–Q^T for plastic solids or $C(t)$–T_z–Q^* for creeping solids based on the formulation are shown to be necessary and efficient to predict the 3D stress fields in the whole forward sector of through-the-thickness cracks.

The empirical formulation obtained in this work provides a set of explicit formulae for the power law plastic and creeping crack tip fields for the first time for both the 2D J dominated HRR and $C(t)$ dominated RR solutions, as well as the 3D J–T_z and $C(t)$–T_z dominated solutions for transition from plane stress to plane strain states. With J and $C(t)$ can be more and more easily calculated by finite element methods and T_z has been formulized for through-the-thickness cracks (Guo, 1995) and surface cracks (Zhao et al. 2008), the explicit formulae presented in this paper should further promote the application of non-linear fracture mechanics.

Acknowledgement

This work is supported by the Aeronautic Science Foundation of China (No. 2010ZA52005).

Appendix A

Fitting formula of $[I_s(T_z,n)]^{1/(n+1)} = A_1 + A_2\exp(-n/A_3) + A_4\exp(-n/A_5)$.

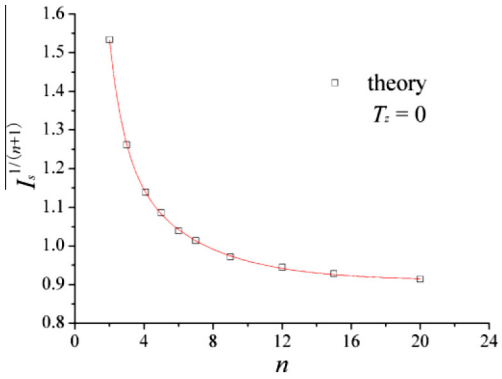

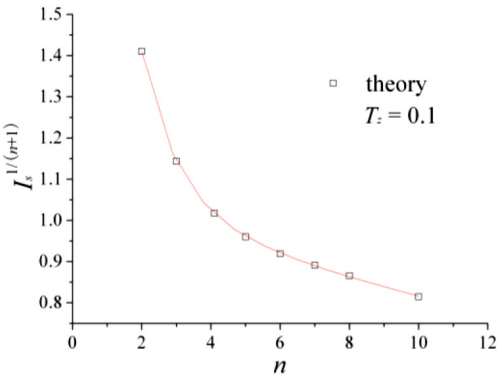

T_z = 0: A_1 = 0.91, A_2 = 3.03728, A_3 = 0.85238, A_4 = 0.53311, A_5 = 4.2471;
T_z = 0.1: A_1 = 0.40836, A_2 = 0.6951, A_3 = 18.77062, A_4 = 2.62364, A_5 = 1.0312.

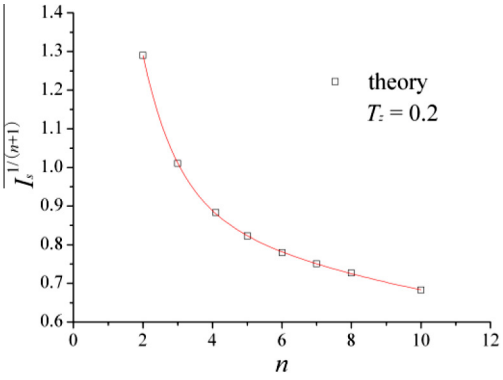

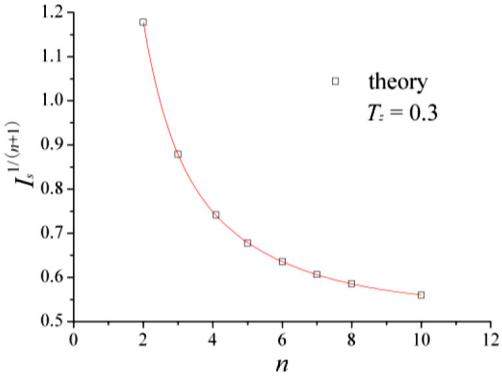

T_z = 0.2: A_1 = 0.53058, A_2 = 2.83816, A_3 = 0.97619, A_4 = 0.49857, A_5 = 8.4655;
T_z = 0.3: A_1 = 0.53458, A_2 = 3.55668, A_3 = 0.76456, A_4 = 0.75134, A_5 = 2.97503.

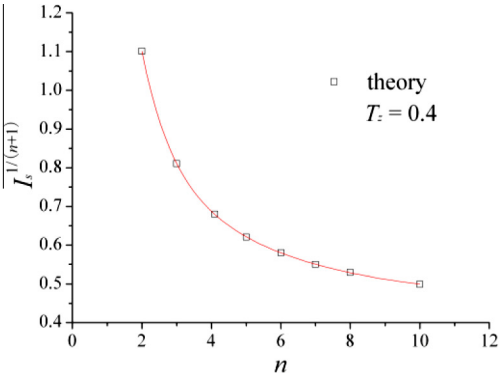

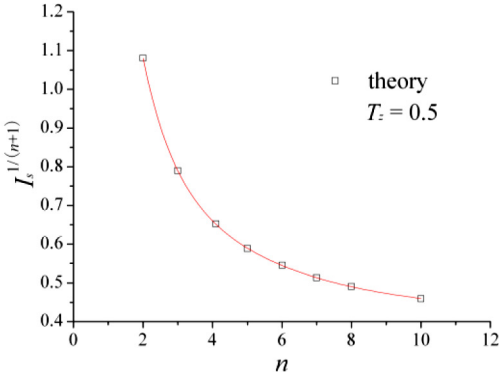

T_z = 0.4: A_1 = 0.45798, A_2 = 0.5895, A_3 = 3.76638, A_4 = 3.3912, A_5 = 0.82034;
T_z = 0.5: A_1 = 0.41917, A_2 = 0.65015, A_3 = 3.60742, A_4 = 3.10925, A_5 = 0.84105.

Appendix B

Fitting formula of $\tilde{\sigma}'_{\theta\theta}(n,\theta) = B_1 + B_2\exp(-n/B_3) + B_4\exp(-n/B_5)$.

B.1. Fitting constants for $\theta = 0°$

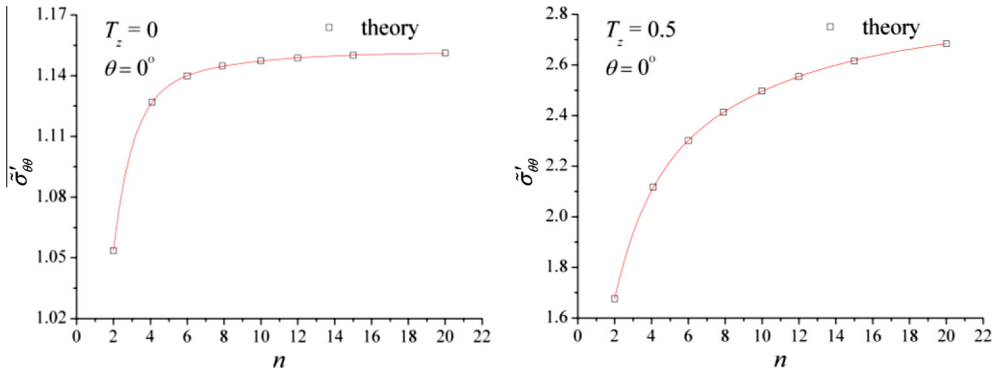

T_z = 0: B_1 = 1.15165, B_2 = −0.0363, B_3 = 4.73231, B_4 = −0.53072, B_5 = 1.01701;
T_z = 0.5: B_1 = 2.76675, B_2 = −0.86155, B_3 = 8.54851, B_4 = −1.35176, B_5 = 1.67481.

B.2. Fitting constants for $\theta = 15°$

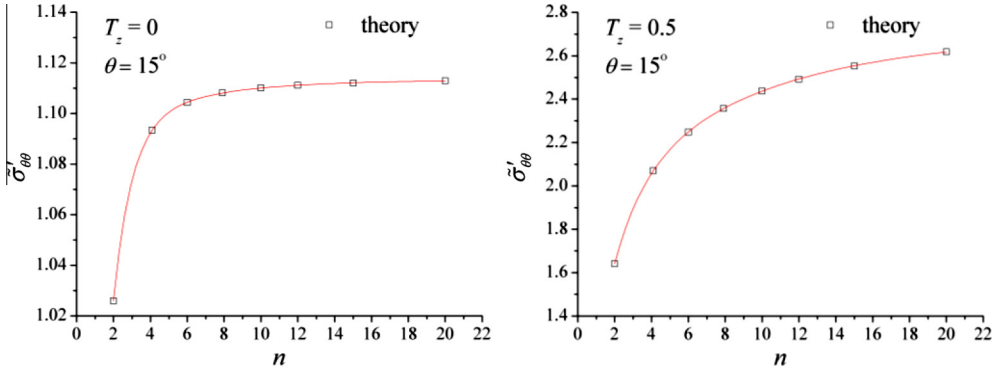

T_z = 0: B_1 = 1.1132, B_2 = −0.52157, B_3 = 0.98973, B_4 = −0.02813, B_5 = 4.56304;
T_z = 0.5: B_1 = 2.69486, B_2 = −1.32295, B_3 = 1.6386, B_4 = −0.84219, B_5 = 8.37302.

B.3. Fitting constants for $\theta = 30°$

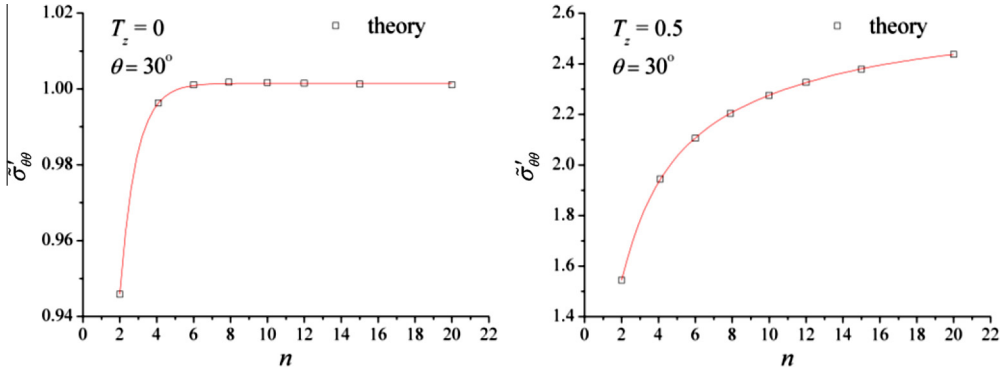

T_z = 0: B_1 = 1.00149, B_2 = −0.26906, B_3 = 0.88119, B_4 = −0.26906, B_5 = 0.88119;
T_z = 0.5: B_1 = 2.50891, B_2 = −1.26399, B_3 = 1.66277, B_4 = −0.73895, B_5 = 8.57408.

B.4. Fitting constants for $\theta = 45°$

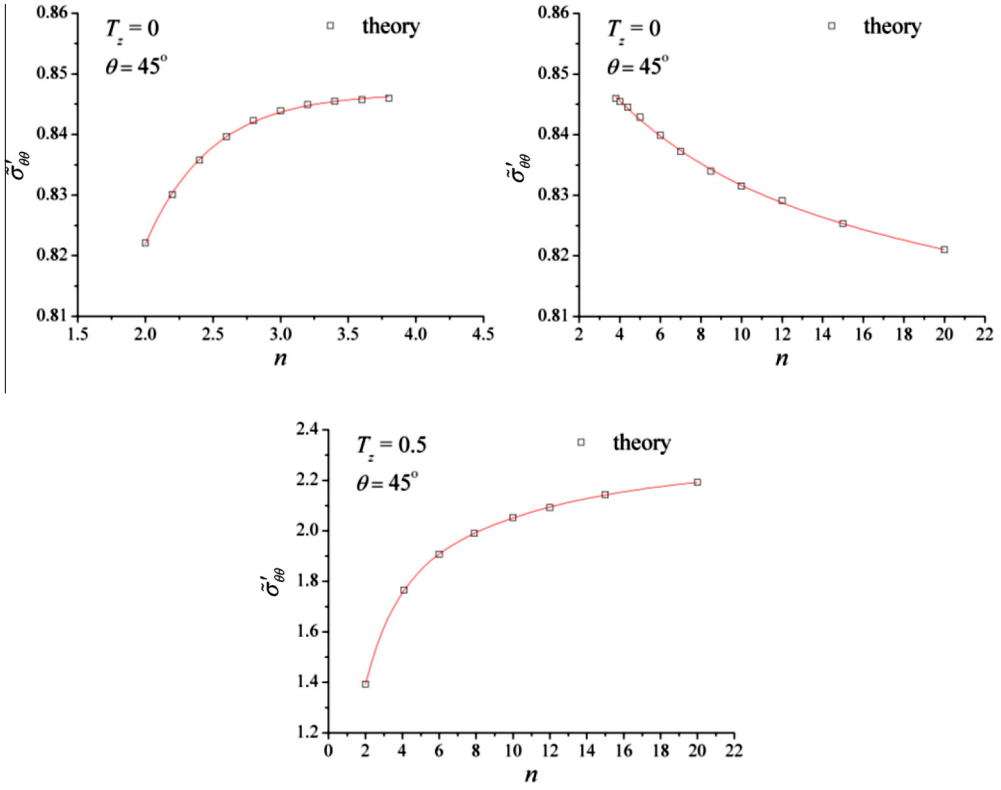

T_z = 0, n < 3.8: B_1 = 0.84683, B_2 = −0.78022, B_3 = 0.48347, B_4 = −0.78, B_5 = 0.48347;
T_z = 0, n > 3.8: B_1 = 0.742, B_2 = 0.03218, B_3 = 6.26389, B_4 = 0.08896, B_5 = 148.044.
T_z = 0.5: B_1 = 2.25543, B_2 = −1.29417, B_3 = 1.52934, B_4 = −0.64655, B_5 = 8.61032.

B.5. Fitting constants for $\theta = 60°$

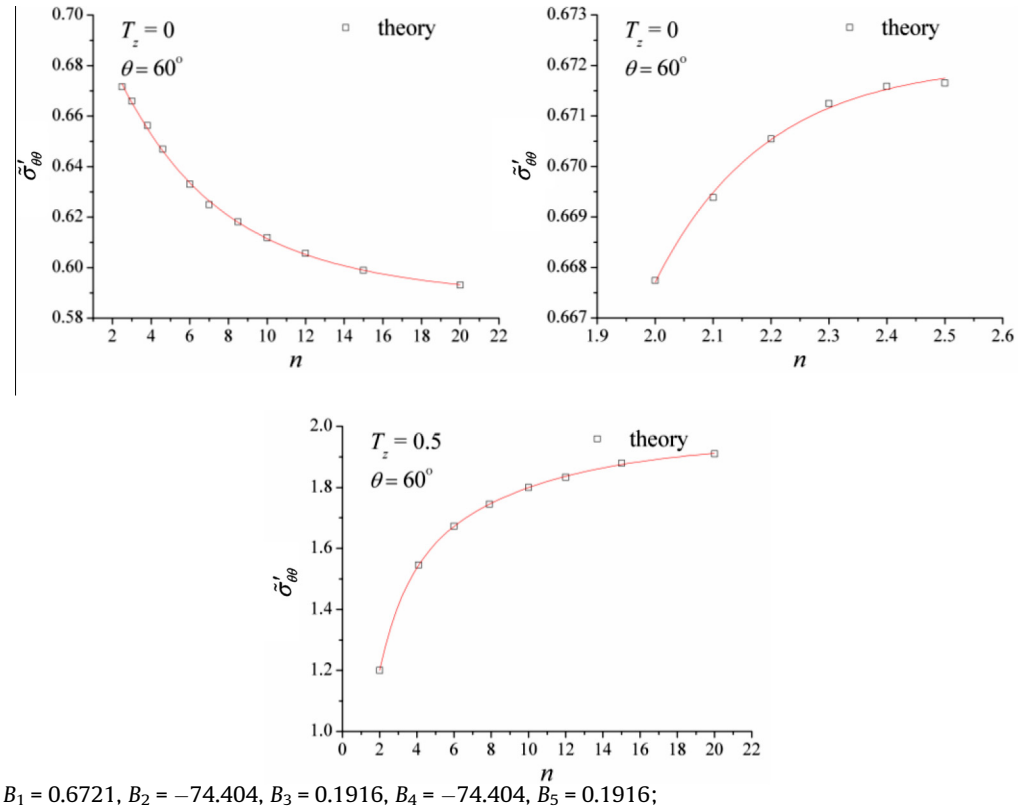

T_z = 0, n < 2.5: B_1 = 0.6721, B_2 = −74.404, B_3 = 0.1916, B_4 = −74.404, B_5 = 0.1916;
T_z = 0, n > 2.5: B_1 = 0.56898, B_2 = 0.12289, B_3 = 5.00469, B_4 = 0.0304, B_5 = 61.9334.
T_z = 0.5: B_1 = 1.94501, B_2 = −1.27904, B_3 = 1.3127, B_4 = −0.62424, B_5 = 6.84834.

B.6. Fitting constants for $\theta = 75°$

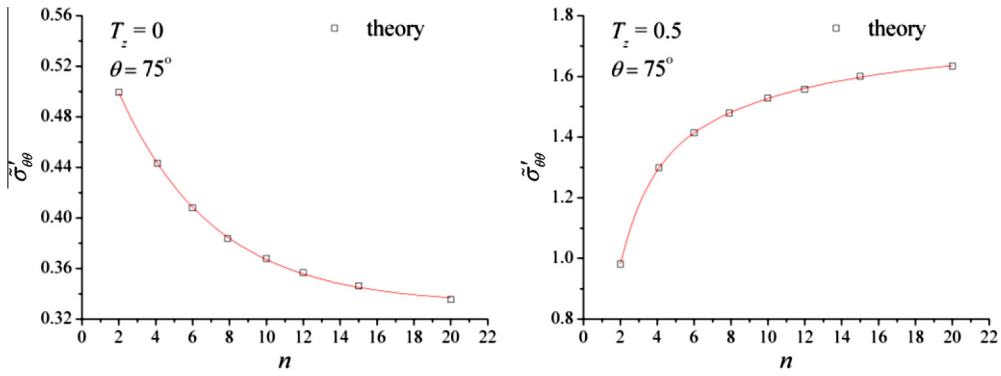

T_z = 0: B_1 = 0.33195, B_2 = 0.12348, B_3 = 5.12709, B_4 = 0.12348, B_5 = 5.12709;
T_z = 0.5: B_1 = 1.67818, B_2 = −0.51781, B_3 = 8.06476, B_4 = −1.17097, B_5 = 1.4439.

B.7. Fitting constants for $\theta = 90°$

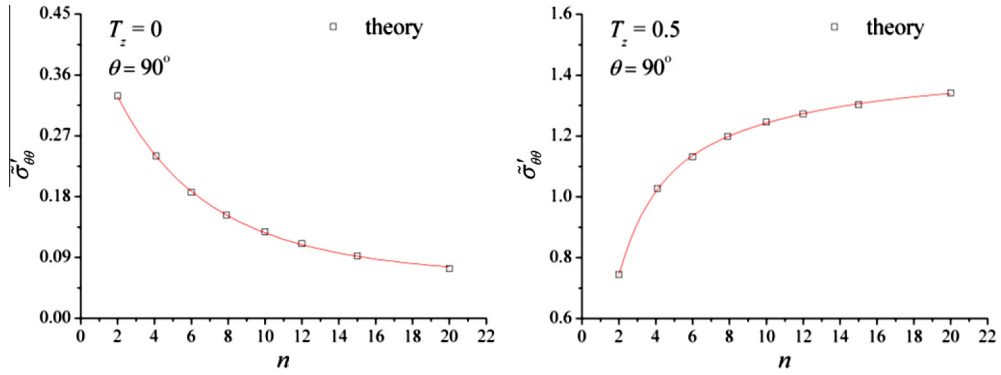

T_z = 0: B_1 = 0.06034, B_2 = 0.1997, B_3 = 7.76211, B_4 = 0.2027, B_5 = 3.43775;
T_z = 0.5: B_1 = 1.38223, B_2 = −0.44699, B_3 = 8.48273, B_4 = −0.93766, B_5 = 1.67441.

Appendix C

Fitting formula of $\tilde{\sigma}'_{rr}(n,\theta) = C_1 + C_2\exp(-n/C_3) + C_4\exp(-n/C_5)$.

C.1. Fitting constants for $\theta = 0°$

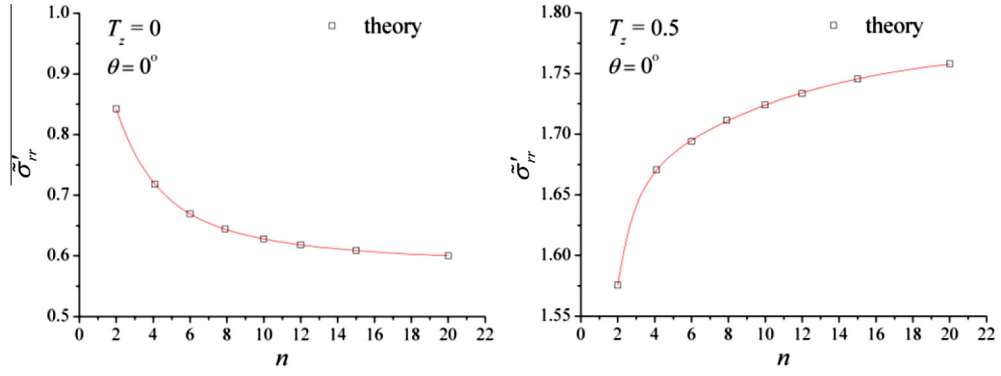

T_z = 0: C_1 = 0.59283, C_2 = 0.14798, C_3 = 6.72276, C_4 = 0.41441, C_5 = 1.84026;
T_z = 0.5: C_1 = 1.77361, C_2 = −0.15409, C_3 = 8.81167, C_4 = −0.78669, C_5 = 0.85265.

C.2. Fitting constants for $\theta = 15°$

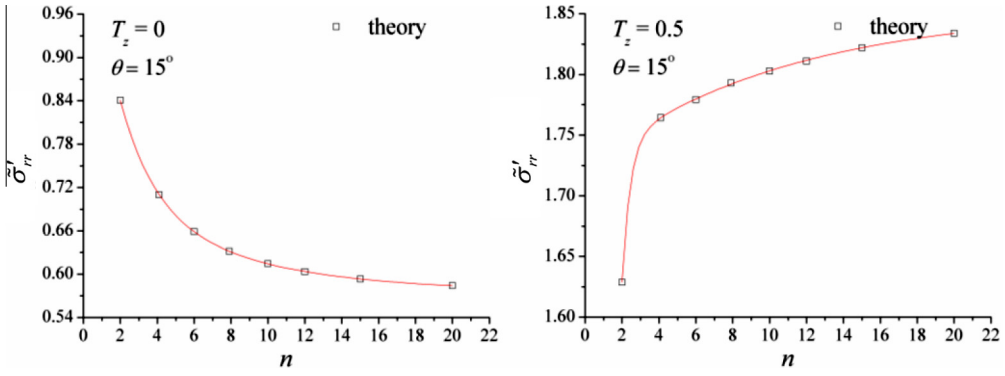

T_z = 0: $C_1 = 0.57571$, $C_2 = 0.42877$, $C_3 = 1.84095$, $C_4 = 0.16169$, $C_5 = 6.77054$;
T_z = 0.5: $C_1 = 1.85348$, $C_2 = -10.81919$, $C_3 = 0.44184$, $C_4 = -0.12991$, $C_5 = 10.57686$.

C.3. Fitting constants for $\theta = 30°$

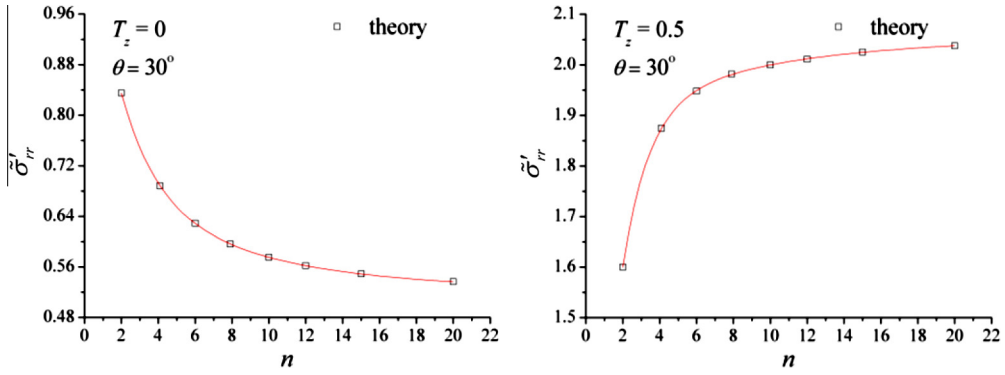

T_z = 0: $C_1 = 0.52367$, $C_2 = 0.47452$, $C_3 = 1.91991$, $C_4 = 0.18882$, $C_5 = 7.4217$;
T_z = 0.5: $C_1 = 2.05232$, $C_2 = -0.18147$, $C_3 = 7.93569$, $C_4 = -1.29978$, $C_5 = 1.39989$.

C.4. Fitting constants for $\theta = 45°$

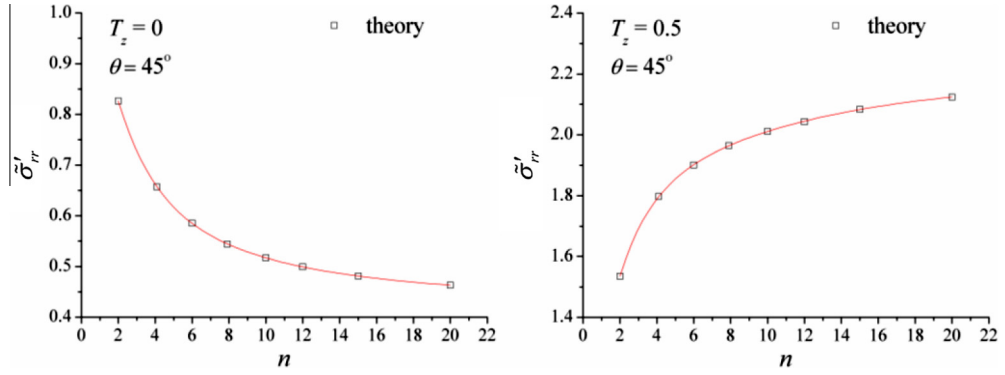

T_z = 0: $C_1 = 0.44223$, $C_2 = 0.52811$, $C_3 = 2.019$, $C_4 = 0.23973$, $C_5 = 8.22613$;
T_z = 0.5: $C_1 = 2.18419$, $C_2 = -0.86697$, $C_3 = 1.60363$, $C_4 = -0.49335$, $C_5 = 9.47041$.

C.5. Fitting constants for $\theta = 60°$

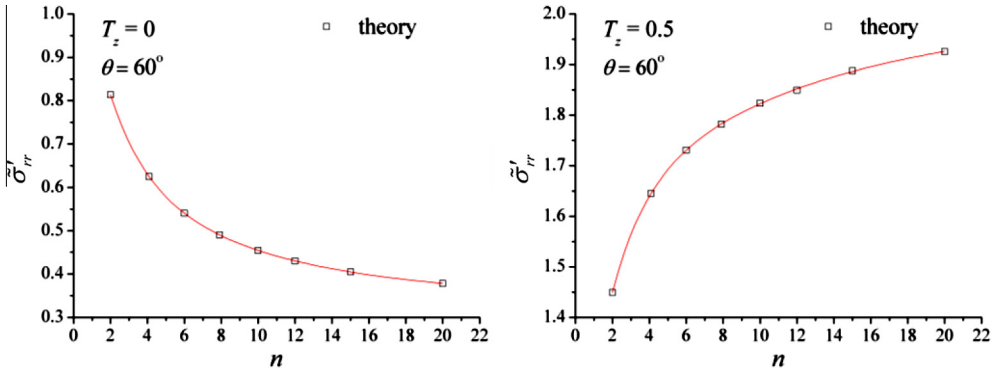

T_z = 0: $C_1 = 0.34651$, $C_2 = 0.54612$, $C_3 = 1.95966$, $C_4 = 0.34257$, $C_5 = 8.44117$;
T_z = 0.5: $C_1 = 1.99782$, $C_2 = -0.41632$, $C_3 = 11.37779$, $C_4 = -0.6052$, $C_5 = 1.79762$.

C.6. Fitting constants for $\theta = 75°$

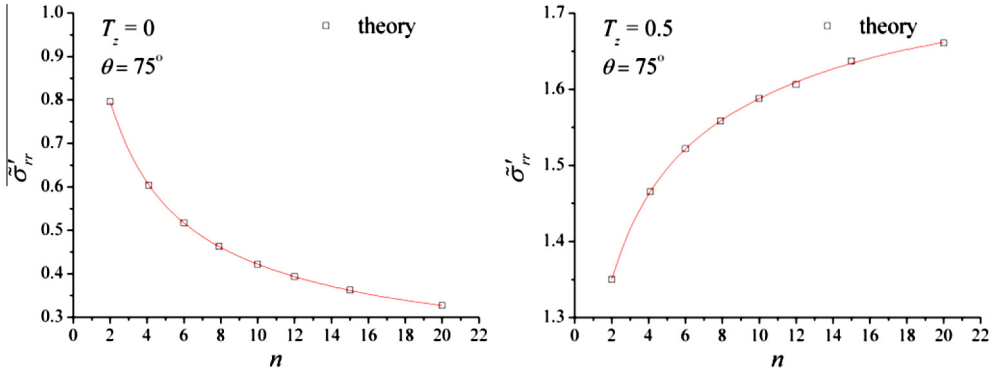

T_z = 0: $C_1 = 0.27717$, $C_2 = 0.54237$, $C_3 = 1.92119$, $C_4 = 0.40358$, $C_5 = 9.58658$;
T_z = 0.5: $C_1 = 1.70378$, $C_2 = -0.31374$, $C_3 = 9.94446$, $C_4 = -0.29585$, $C_5 = 1.79598$.

C.7. Fitting constants for $\theta = 90°$

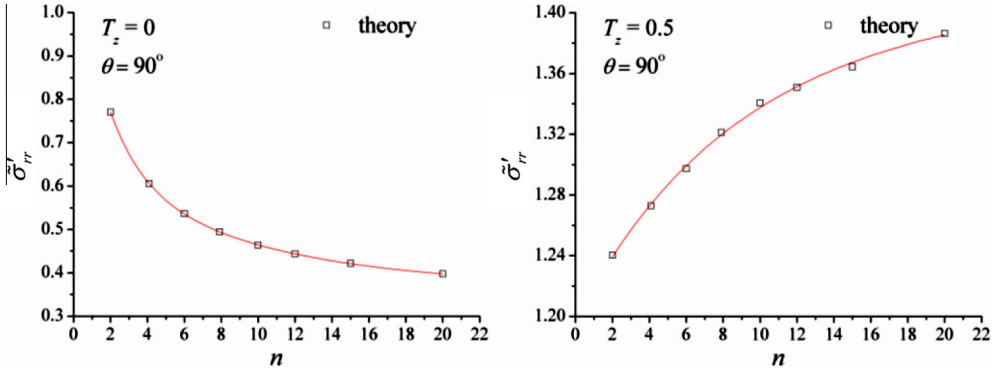

T_z = 0: $C_1 = 0.36867$, $C_2 = 0.2999$, $C_3 = 8.60638$, $C_4 = 0.50095$, $C_5 = 1.7931$;
T_z = 0.5: $C_1 = 1.45$, $C_2 = -0.18212$, $C_3 = 8.19242$, $C_4 = -0.0706$, $C_5 = 53.94641$.

Appendix D

Fitting formula of $\tilde{\sigma}'_{r\theta}(n,\theta) = D_1 + D_2\exp(-n/D_3) + D_4\exp(-n/D_5)$.

D.1. Fitting constants for $\theta = 0°$

$\tilde{\sigma}'_{r\theta}(n,0) \equiv 0$.

D.2. Fitting constants for $\theta = 15°$

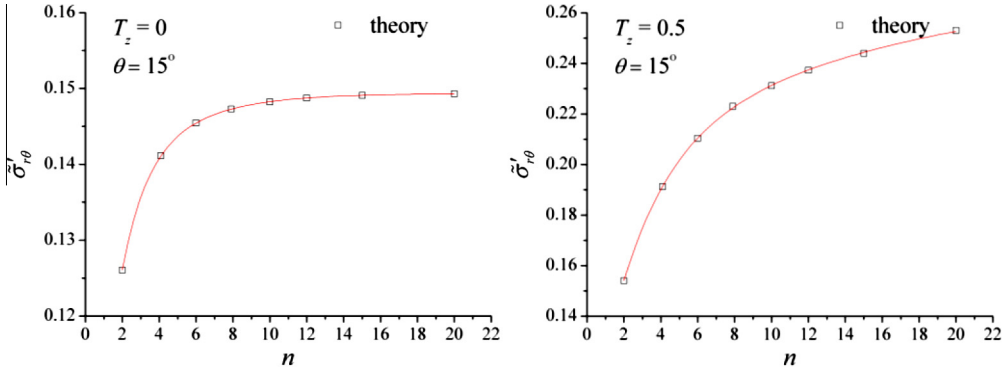

T_z = 0: D_1 = 0.14935, D_2 = −0.06158, D_3 = 1.25408, D_4 = −0.01922, D_5 = 3.46106;
T_z = 0.5: D_1 = 0.275, D_2 = −0.07555, D_3 = 16.36786, D_4 = −0.11419, D_5 = 2.67978.

D.3. Fitting constants for $\theta = 30°$

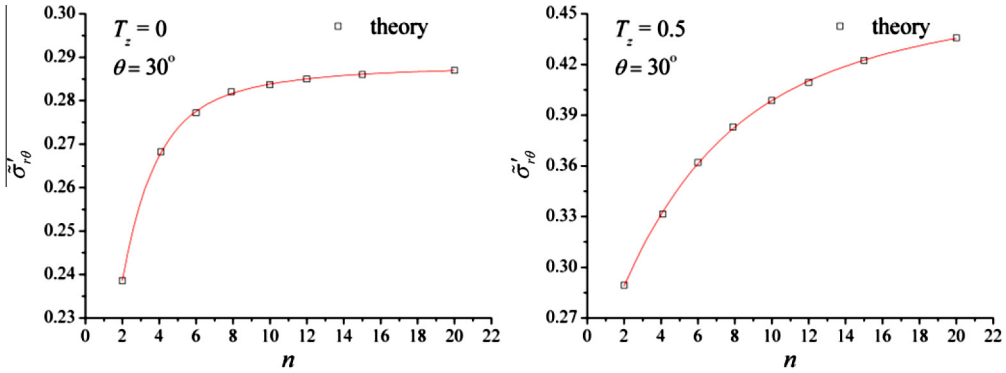

T_z = 0: D_1 = 0.28757, D_2 = −0.01945, D_3 = 5.80126, D_4 = −0.11831, D_5 = 1.64945;
T_z = 0.5: D_1 = 0.485, D_2 = −0.07624, D_3 = 38.367, D_4 = −0.17985, D_5 = 5.33992.

D.4. Fitting constants for $\theta = 45°$

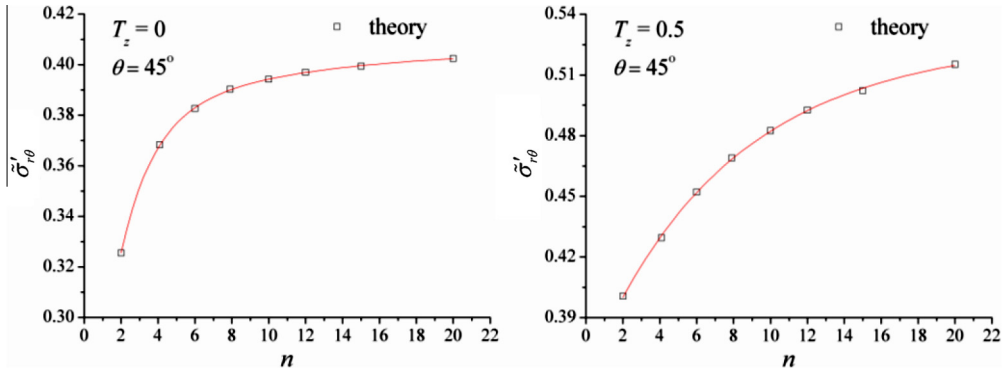

T_z = 0: D_1 = 0.40575, D_2 = −0.16437, D_3 = 1.74411, D_4 = −0.03541, D_5 = 8.53798;
T_z = 0.5: D_1 = 0.5352, D_2 = −0.02033, D_3 = 32.49193, D_4 = −0.15326, D_5 = 7.17591.

D.5. Fitting constants for $\theta = 60°$

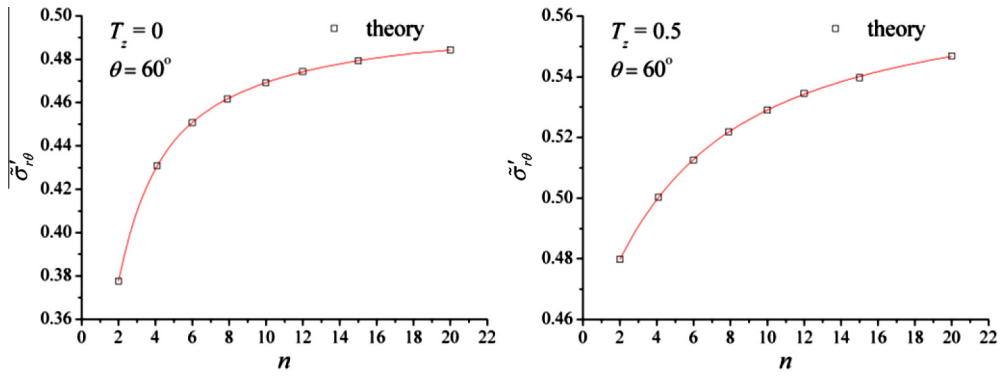

T_z = 0: $D_1 = 0.48918$, $D_2 = -0.07906$, $D_3 = 7.16785$, $D_4 = -0.18308$, $D_5 = 1.58124$;
T_z = 0.5: $D_1 = 0.5612$, $D_2 = -0.05763$, $D_3 = 14.2851$, $D_4 = -0.05407$, $D_5 = 3.66856$.

D.6. Fitting constants for $\theta = 75°$

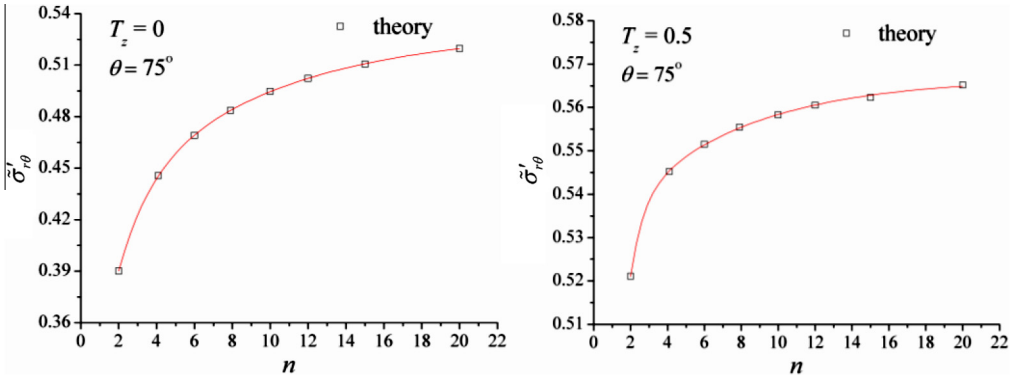

T_z = 0: $D_1 = 0.5307$, $D_2 = -0.16685$, $D_3 = 1.64882$, $D_4 = -0.11515$, $D_5 = 8.55068$;
T_z = 0.5: $D_1 = 0.56673$, $D_2 = -0.03812$, $D_3 = 6.57695$, $D_4 = -0.3039$, $D_5 = 0.70142$.

D.7. Fitting constants for $\theta = 90°$

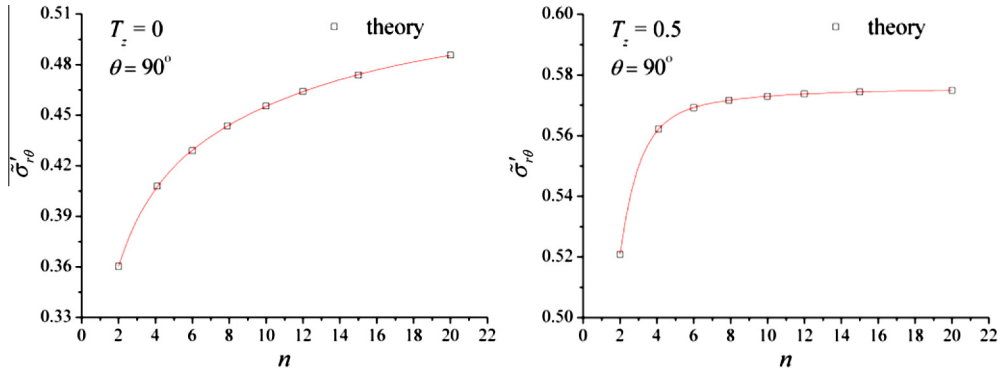

T_z = 0: $D_1 = 0.50308$, $D_2 = -0.129$, $D_3 = 10.04338$, $D_4 = -0.13416$, $D_5 = 1.55519$;
T_z = 0.5: $D_1 = 0.57521$, $D_2 = -0.01812$, $D_3 = 4.77617$, $D_4 = -0.30666$, $D_5 = 1.01106$.

References

Betegon, C., Hancock, J., 1991. Two-parameter characterization of elastic–plastic crack-tip fields. J. Appl. Mech. 58, 104–113.

Budden, P.J., Ainsworth, R.A., 1997. The effect of constraint on creep fracture assessments. Int. J. Fract. 87, 139–149.

Graba, M., Galkiewicz, J., 2007. Influence of the crack tip model on results of the finite elements method. J. Theor. Appl. Mech. 45, 225–237.

Guo, W., 1993a. Elastoplastic three dimensional crack border field – I. Singular structure of the field. Eng. Fract. Mech. 46, 93–104.

Guo, W., 1993b. Elastoplastic three dimensional crack border field – II. Asymptotic solution for the field. Eng. Fract. Mech. 46, 105–113.

Guo, W., 1995. Elasto-plastic three-dimensional crack border field – III. Fracture parameters. Eng. Fract. Mech. 51, 51–71.

Guo, W., 2000. Recent advances in three-dimensional fracture mechanics. Key Eng. Mater. 183, 193–198.

Hutchinson, J., 1968. Singular behaviour at the end of a tensile crack in a hardening material. J. Mech. Phys. Solids 16, 13–31.

Leevers, P., Radon, J., 1982. Inherent stress biaxiality in various fracture specimen geometries. Int. J. Fract. 19, 311–325.

Li, Y.C., Wang, Z.Q., 1986. High-order asymptotic field of tensile plane–strain nonlinear crack problems. Sci. Sin. (Ser. A) 29, 941–955.

McMeeking, R., 1977. Finite deformation analysis of crack-tip opening in elastic-plastic materials and implications for fracture. J. Mech. Phys. Solids 25, 357–381.

Nakamura, T., Parks, D., 1990. Three-dimensional crack front fields in a thin ductile plate. J. Mech. Phys. Solids 38, 787–812.

Nguyen, B., Onck, P., van der Giessen, E., 2000a. Crack-tip constraint effects on creep fracture. Eng. Fract. Mech. 65, 467–490.

Nguyen, B., Onck, P., van der Giessen, E., 2000b. On higher-order crack-tip fields in creeping solids. J. Appl. Mech. 67, 372–382.

O'Dowd, N., Shih, C., 1991. Family of crack-tip fields characterized by a triaxiality parameter – I. Structure of fields. J. Mech. Phys. Solids 39, 989–1015.

O'Dowd, N., Shih, C., 1992. Family of crack-tip fields characterized by a triaxiality parameter – II. Fracture applications. J. Mech. Phys. Solids 40, 939–963.

Rice, J., 1968. A path independent integral and the approximate analysis of strain concentration by notches and cracks. J. Appl. Mech. 35, 379–386.

Rice, J., Rosengren, G., 1968. Plane strain deformation near a crack tip in a power-law hardening material. J. Mech. Phys. Solids 16, 1–12.

Riedel, H., Rice, J., 1980. Tensile cracks in creeping solids. In: Fracture Mechanics: Twelfth Conference, ASTM STP 700, pp. 112–130.

Ritchie, R., Knott, J., Rice, J., 1973. On the relationship between critical tensile stress and fracture toughness in mild steel. J. Mech. Phys. Solids 21, 395–410.

Ritchie, R., Thompson, A., 1985. On macroscopic and microscopic analyses for crack initiation and crack growth toughness in ductile alloys. Metall. Mater. Trans. A. 16, 233–248.

Xia, L., Wang, T., Shih, C., 1993. Higher-order analysis of crack tip fields in elastic power-law hardening materials. J. Mech. Phys. Solids 41, 665–687.

Xiang, M., Yu, Z., Guo, W., 2011. Characterization of three-dimensional crack border fields in creeping solids. Int. J. Solids. Struct. 48, 2695–2705.

Yang, S., Chao, Y., Sutton, M., 1993. Higher order asymptotic crack tip fields in a power-law hardening material. Eng. Fract. Mech. 45, 1–20.

Zhao, J., Guo, W., She, C., 2008. Three-parameter approach for elastic–plastic fracture of the semi-elliptical surface crack under tension. Int. J. Mech. Sci. 50, 1168–1182.